

## Development of models for Attitude Determination and Control System components for CubeSat applications



Edgard Martínez Vidal

**Space Engineering, master's level (120 credits)**  
**2017**

Luleå University of Technology  
Department of Computer Science, Electrical and Space Engineering



# Abstract

## Master Thesis

Development of models for Attitude Determination and Control System components for CubeSat applications.

by Edgard Martínez

Master Programme in Spacecraft Design

Luleå University of Technology

2017

In this Master Thesis, numerical models of ADCS components are performed. The models will be used in the design of the first 3U CubeSat of the CSU Montpellier, the ROBUSTA 3-A. The goal of the thesis is to develop numerical models of angular rate sensors and reaction wheels and to obtain relevant information of these components in the context of the R-3A mission.

Firstly, the state-of-the art of models are outlined, and the most suitable are chosen. Secondly, assumptions are made, and the models are implemented. Next, the models are parametrized for specific elements to be used on R-3A. Lastly, the models are validated and simulated.

The results of simulations confirm a choice of the CoTS components for the R3A mission. Besides, the results provide information about system performance parameters such as RW acceleration time, maximum satellite speed, and attitude knowledge accuracy in eclipse.

# Acknowledgments

Foremost, I would like to thank my supervisor Dr Andrey Khorev for getting the opportunity to carry out my master thesis at the CSU Montpellier, his support and guide throughout the thesis

General thanks to everyone at the CSU Montpellier that helped me during my work there. Thanks to my examiner Dr Leonard Felicetti for his support.

Then I am very grateful to my family, who made all this possible. Finally, I would like to thank my couple Claudia for her support and her patience.

This study has been conducted with the financial support of the Van Allen Foundation.

This thesis has been co-funded by the Erasmus Programme of the European Union.

# Table of Contents

<b>ABSTRACT .....</b>	<b>2</b>
<b>ACKNOWLEDGMENTS .....</b>	<b>3</b>
<b>TABLE OF CONTENTS .....</b>	<b>4</b>
<b>LIST OF FIGURES .....</b>	<b>5</b>
<b>LIST OF TABLES .....</b>	<b>7</b>
<b>NOMENCLATURE .....</b>	<b>8</b>
<b>CHAPTER 1 .....</b>	<b>9</b>
1.1. THESIS OUTLINE.....	9
1.2. UNIVERSITY SPACE CENTER OF MONTPELLIER.....	9
1.3. ROBUSTA 3A MÉDITERRANÉE .....	11
<b>CHAPTER 2 .....</b>	<b>13</b>
2.1. ADCS SIMULATION SETUP OVERVIEW .....	13
2.2. ANGULAR RATE SENSOR MODEL .....	15
2.3. REACTION WHEEL MODEL.....	17
<b>CHAPTER 3 .....</b>	<b>22</b>
3.1. IMPLEMENTING ANGULAR RATE SENSOR MODEL .....	22
3.1.1. <i>Sensing element model</i> .....	22
3.1.2. <i>Analogue filter model</i> .....	23
3.1.3. <i>Analogue to digital converter model</i> .....	23
3.1.4. <i>Additional filters model</i> .....	24
3.2. IMPLEMENTING REACTION WHEEL MODELS .....	25
3.2.1. <i>“Open loop” model of RW</i> .....	25
3.2.2. <i>Speed control model</i> .....	27
3.2.3. <i>Simplified reaction wheel model</i> .....	28
3.3. IMPLEMENTING SATELLITE DYNAMIC MODEL.....	29
<b>CHAPTER 4 .....</b>	<b>32</b>
4.1. ANGULAR RATE SENSOR SIMULATIONS.....	32
4.1.1. <i>Model parametrization</i> .....	32
4.1.2. <i>Verification model</i> .....	32
4.1.3. <i>Angular rate sensor performance relative to a long term (satellite in eclipse)</i> ..	34
4.2. REACTION WHEEL SIMULATIONS.....	36
4.2.1. <i>Parameters</i> .....	36
4.2.2. <i>Simulations with “open-loop” model of RW</i> .....	36
4.2.3. <i>Simulations with speed control model of RW</i> .....	39
4.2.4. <i>Verification simplified model</i> .....	41
4.3. RW-SATELLITE SYSTEM DYNAMICS SIMULATIONS .....	42
<b>CHAPTER 5 .....</b>	<b>45</b>
<b>CHAPTER 6   WORKS CITED .....</b>	<b>46</b>
<b>APPENDIX A.....</b>	<b>49</b>
<b>APPENDIX B.....</b>	<b>52</b>
<b>APPENDIX C.....</b>	<b>53</b>

# List of Figures

Figure 1-1: Logo Robusta-1A .....	10
Figure 1-2: Logo Robusta-1B .....	10
Figure 1-3: Logo MT-Cube.....	10
Figure 1-4: Logo Celesta.....	11
Figure 1-5: Logo Robusta-3A .....	11
Figure 1-6: Robusta-3A CubeSat mechanical design view (left) and simulated view (right) .....	11
Figure 1-7: ADCS mechanical design view.....	12
Figure 2-1: Architecture block diagram of an ADCS simulator setup .....	14
Figure 2-2: Sensors used to obtain the state vector.....	15
Figure 2-3: Friction torque model used in [16].....	17
Figure 2-4: Torque ripple generated by PMAC motor [17] .....	18
Figure 2-5: Speed control configuration for a BLDC motor [19].....	18
Figure 2-6: Simulink implementation of a RW model [20].....	19
Figure 2-7: PMAC motor with concentrated winding (left) and with distributed winding (right) [23].....	19
Figure 2-8: Trapezoidal Back EMF from BLDCM [24].....	19
Figure 2-9: Sinusoidal Back EMF from PMSM [24]. .....	20
Figure 3-1: Black box model gyroscope .....	22
Figure 3-2: Sensor signal chain modules .....	22
Figure 3-3: ADC Simulink model.....	24
Figure 3-4: Black box of reaction wheel model.....	25
Figure 3-5: measured real back EMF waveform of BLDC motor [48]. .....	25
Figure 3-6: Architecture “Open loop” model of reaction wheel.....	26
Figure 3-7: 3-phase inverter circuit.....	26
Figure 3-8: Architecture Speed control model of reaction wheel .....	28
Figure 3-9: Speed controller configuration.....	28
Figure 3-10: Satellite dynamics black box model.....	29
Figure 4-1: Allan variance datasheets ADIS16135 (left) Gypro2300 (right) .....	33
Figure 4-2: Allan variance model ADIS16135 .....	33
Figure 4-3: Allan variance model Gypro2300 .....	33
Figure 4-4: ADIS16135 angular position results for 45 minutes with zero-rate input .....	34
Figure 4-5: CRM200 angular position results for 45 minutes with zero-rate input .....	35
Figure 4-6: GYPRO2300 angular position results for 45 minutes with zero-rate input .....	35
Figure 4-7: Expected current waveforms and torque with trapezoidal commutations [19]. .....	37

Figure 4-8: Current, back EMF and torque for open loop model .....	37
Figure 4-9: Hall sensor signals.....	38
Figure 4-10: Control switching signals clockwise rotation .....	38
Figure 4-11: Open loop results with RW motor .....	39
Figure 4-12: Open loop results of maxon motor.....	39
Figure 4-13: Current, back EMF and torque for speed controller model .....	40
Figure 4-14: Zoomed view from Figure 4-13 .....	40
Figure 4-15: Open loop results of speed controller model.....	41
Figure 4-16: Results simplified RW model .....	41
Figure 4-17: Results Scenario-1 of RW-Satellite system .....	42
Figure 4-18: Results Scenario-2 of RW-Satellite system .....	43
Figure 4-19: Results Scenario-3 of RW-Satellite system .....	43
Figure 4-20: Results Scenario-4 of RW-Satellite system .....	44
Figure 4-21: Results Scenario-1 of RW-Satellite system with detailed RW .....	44

# List of Tables

Table 1: Clockwise rotation switches sequence.....	27
Table 2: Counter-clockwise rotation switches sequence .....	27
Table 3: Gyroscopes parameters used in the mathematical model .....	32
Table 4: Parameters used with detailed RW model .....	36
Table 5: Parameters used with simplified RW model.....	36
Table 6: Parameters for different scenario RW-Sat system simulations. ....	42



# Nomenclature

## Acronyms

ADC	Analog to Digital Converter
ADCS	Attitude Determination and Control System
ARS	Angular rate sensor
ARW	Angular random walk
BLDC	Brushless direct current
BLDCM	Brushless direct current motor
BRF	Body reference frame
CERN	European Organization for Nuclear Research
CoTS	Components off the shelf
CSU	Centre spatial universitaire
CVGs	Coriolis vibratory gyros
EMF	Electromotive force
EPS	Electrical Power system
ESA	European space agency
FIR	Finite impulse response
FOC	Field oriented control
FOG	Fibre optic gyroscope
LIRMM	Laboratoire d'Informatique, de Robotique et de Microélectronique de Montpellier
MEMS	Microelectromechanical System
MW	Momentum wheels
OBDH	On-board data handling
PID	Proportional–Integral–Derivative controller
PMAC	Permanent magnet alternating current
PMS	Permanent magnet synchronous
PMSM	Permanent magnet alternating current
PWM	Pulse width modulation
R-3A	Rebusta-3a
RADIAC	Radiation and Components
RND	Rate noise density
ROBUSTA	Radiation On Bipolar for University Satellite Test Application
RRW	Rate random walk
RW	Reaction wheel
STRM	Spacecraft structure and mechanisms
SWaP	Size, weight, and power constraints (so-called “” constraints)
TT&C	Telemetry, tracking and command
MTQ	Magnetorquer

---

# CHAPTER 1

---

## Introduction

In the year 2013, the University Space Center (USC) of Montpellier started the project to build its first 3-Units CubeSat; the ROBUSTA-3A (R-3A). To accomplish the requirements of the payload, the satellite needs an Attitude determination and control system (ADCS). Presently, to design and develop the ADCS, the CSU is developing a CubeSat's ADCS simulation setup to analyse the behaviour of ADCS components and the system as a whole. The tool can be used for control algorithm development and optimisation, during tests and validation, and later for satellite operation planning. The simulator has to include all the elements that made up the ADCS and all the elements that interact with it. Each of these elements are numerically modeled independently as a black box and later are interconnected. These models have to emulate the respective element well enough to be able to build adequate control algorithm and have a realistic expectation of ADCS performance. This thesis contributes to the development of the ADCS simulator of the CSU by developing numerical models of ADCS components. The goal is to develop numerical models of angular rate (ARS) sensors and reaction wheels and to obtain relevant information of these components in the context of the R-3A mission. The steps followed in this report to get the goals are:

- Evaluate different models to identify the one that might be suitable
- Develop the numerical model
- Parametrize the model for specific element to be used on R3A
- Verify the correctness of the developed model
- Simulate the model in the context of the R-3A mission and analyze the results.

### 1.1. Thesis outline

This report is composed of 5 chapters, in the current and first chapter, the introduction and the objectives of the report are presented together with information on the University Space center of Montpellier and its satellites. CHAPTER 2 describes and summarise mathematical models of angular rate sensors and reaction wheels that can be found in the literature. CHAPTER 3 gives the mathematical models developed of angular rate sensor, reaction wheels and the satellite dynamics, as well as the assumptions that have been taken. CHAPTER 4 presents the different scenarios used in the simulations and their results. CHAPTER 5 presents the conclusions done.

### 1.2. University Space Center of Montpellier

The University Space Center of Montpellier is a division of the University of Montpellier and the first French university space center. Its purpose is to educate students in space sciences through the design, production, and testing of nanosatellites. The CSU was created in 2011 to consolidate nanosatellite activities that were initiated in 2006 by the RADIAC (radiation and components) team of the Institute of electronics (IES), a research institute also affiliated with the university. In 2006, the University of Montpellier was accepted for the CNES EXPRESSO program with ROBUSTA (Radiation On Bipolar for University Satellite Test Application) project, a real CubeSat mission with the satellite built by students. In 2012, CSU launched the nanosatellite Robusta-1A, the first French nanosatellite put into orbit, and it began a strong partnership with the Van Allen Foundation. The Foundation provides strategic and financial support to the CSU. Finally, in December 2015, the CSU was installed in its new premises on the Saint Priest campus in Montpellier. This new building makes it possible to bring together all the actors of the projects as well as all the necessary equipment. Since the launch of Robusta-1A, CSU has been developing

5 CubeSats, following a summary of their mission and the current status of the satellites are given [1].

**ROBUSTA-1A**, a 1 “U” CubeSat, was the first satellite built by students at the University of Montpellier. The development of this satellite began in 2006 and was launched in 2012 by the Vega launcher, maiden flight. The mission of the Robusta-1A was to measure the effect of radiation on components made up of bipolar transistors to validate a test method proposed by the RADIAC team. A total of 300 students participated in this project.



*Figure 1-1: Logo Robusta-1A*

**ROBUSTA-1B** is an upgrade version of Robusta-1A with new quality assurance procedures intended to enable CSU to validate a new standard 1-U CubeSat platform, dubbed Robusta-1U. 50 students of the CSU participated in its development that had started in 2012 and had been ready to be launched in 2015 but finally was launched in June of 2017 .



*Figure 1-2: Logo Robusta-1B*

The **MT Cube** is a Nanosatellite on behalf of the ESA which platform is provided by the CSU and the payload by the LIRMM. The expected duration of the project is of two years from 2014 and ready for launch in 2017. The satellite will test the hardness of several types of memory against space radiation: Flash memory, SRAM, MRAM and FRAM



*Figure 1-3: Logo MT-Cube*

**Celesta** (CERN Latchup Experiment and STudent sAtellite) nanosatellite project is a collaboration between the CERN which provides the payload, the CSU which provides the platform and the ESA fly your satellite program that finances the launch. The planned development time is of 3 years from 2015 to 2018. The satellite's mission is to compare radiative environments in low orbit using CERN's radiation monitor (the RADMON detector).



Figure 1-4: Logo Celesta

### 1.3. ROBUSTA 3A Méditerranée

The ROBUSTA-3A (R-3A) satellite is the first 3-unit CubeSat under development by the CSU Montpellier. The project was initiated in 2013, and the satellite is expected to be launched in 2020.



Figure 1-5: Logo Robusta-3A

The satellite mission is to collect meteorological data from the ship based terminals in the Mediterranean Sea, and to deliver it to Mateo France within 90 minutes from the last measurement, enabling to improve the forecasting of Cevennes. The payload is S-band antenna and associated electronics. The designed orbit is a Sun Synchronous orbit at 615 km with  $98.2^\circ$  of inclination.

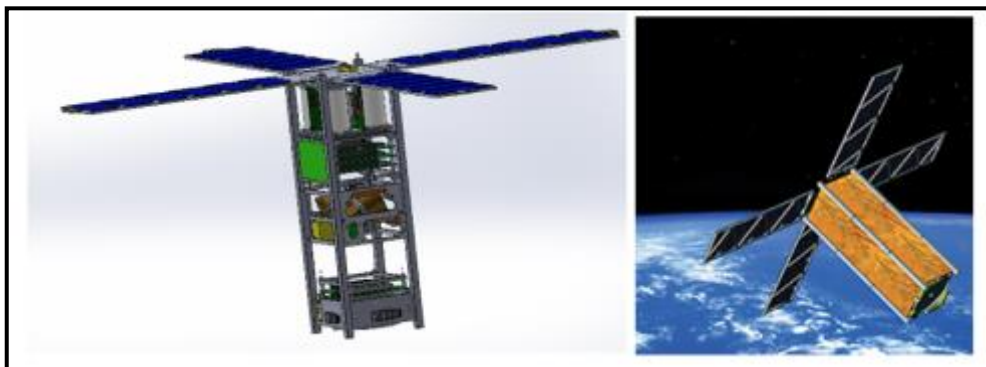
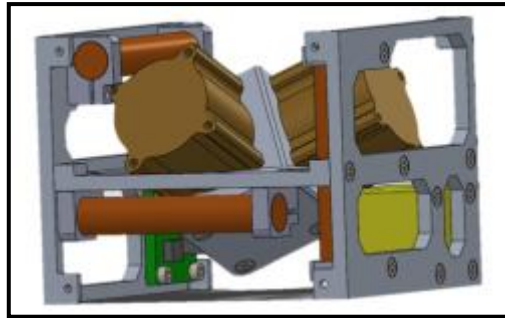


Figure 1-6: Robusta-3A CubeSat mechanical design view (left) and simulated view (right)

The different subsystems of the satellite are:

- The **Electrical Power system (EPS)**, provides, stores, regulates, and distributes electrical power to the systems in the satellite. The EPS consists of 4 deployable solar panels in flower configuration, batteries, and a power control and distribution unit.
- The **telemetry, tracking and command (TT&C)** system, is used to communicate with, track, and give commands to the spacecraft to monitor and control the orbit, attitude and health of the spacecraft. The system consists of an uhf-band antenna, transmitters, receivers, filters, amplifiers, controlling computer, and harnesses.
- The **on-board data handling (OBDH)** system is responsible for collecting, processing, routing and storing on-board generated data and for routing and storing uplinked data.

- The **spacecraft structure** and mechanisms (STRM) includes the frames of the satellite the mechanical adapters for the payload and subsystems. Mechanisms for deployment of antennas and solar panels.
- The **thermal control system** maintains the subsystems to an adequate operational range temperature and is dimensioned to withstand the worst-case thermal loads. The satellite will be affected by the sunlight and the thermal and solar radiation reflected from Earth. It is also affected by the temperature gradients as the satellite travels in and out of the earth's shadow. The subsystems include radiators and heaters along with Multilayer insulation (MLI).
- ADCS is responsible for the attitude determination, pointing and stabilization of the satellite and performing maneuvers according to the mission profile. The components that forms the ADCS can be seen in Figure 1-7 and are listed below:
  - 3 Small wheels (CubeSpace) on Pyramidal support
  - 3 Magnetorquers (CubeSpace)
  - 3 Magnetometers (1 axis: Micromag3)
  - 3 angular rate sensors (1-axis: GYPRO2300)
  - 1 ADCS controller based on NanoMind A3200 by GomSpace.



*Figure 1-7: ADCS mechanical design view*

---

## CHAPTER 2

---

# Literature review

The design of the ADCS in CubeSats is an ambitious task due that the size, weight, and power constraints (so-called “SWaP” constraints) are severe. Sensors and actuators must be made to fit within the limited size, weight, and power specifications while still performing to high accuracies for many small vehicle mission applications [2].

The attitude determination system processes sensor data to form an estimate of the satellite’s attitude. Sensors typically used in CubeSats are sun sensors, magnetometers or angular rate sensors. While not in eclipse, CubeSats use Sun sensors and magnetometers together with Sun and satellite ephemerids and a model of the magnetic field on-board to provide 3-axis attitude of the satellite. However, in eclipse and without the sun sensors, angular rate sensors may be used to update the 3-axis attitude knowledge. ARS are inertial sensors that estimate the attitude by measuring the rate of rotation of the spacecraft [3]. In this thesis, the terms angular rate sensor, gyroscope and gyro are interchangeable. Gyros can be classified by the physical mechanisms they use: spinning-mass gyros, optical gyros, or Coriolis vibratory gyros (CVGs) [4]. In CubeSat, as a result of the SWaP constraints, only CVGs are appropriate for CubeSat applications. CVGs are commonly manufactured with microelectromechanical system (MEMS) technology, and hence they are known as MEMS gyros.

The satellite’s orientation estimated by the attitude determination system is compared with the desired attitude by the control system. If there is a difference between two attitudes the control system commands the actuators to create a torque to change the attitude of the satellite. In CubeSats, these actuators commonly are Momentum-exchange devices and magnetorquers. Momentum-exchange devices provide smooth changes in torque, allowing very accurate pointing of the satellite [5]. Momentum exchange devices can be distinguished according to its mode of operation as momentum wheels [MW] and reaction wheels [RW]. MW spin at a predefined nominal angular velocity to provide spin stabilization and operate with small variations around this reference velocity. RW typically have zero nominal angular speed and changes its velocity to absorb the external disturbances or to implement slew manoeuvre. However, both terms MW and RW can be used interchangeably to a certain extent, and for CubeSat, the RW term is more common. Thus, in this report, momentum-exchange devices will be named reaction wheels for simplicity.

## 2.1. ADCS simulation setup overview

Evaluate the performance of the control and estimation algorithms for Satellites requires the use of a realistic simulator that represents the behaviour of the system accurately. The ADCS simulation setup that is being developed by the CSU will provide a realistic simulator able to develop and optimize control algorithm, during tests and validation, and later for satellite operation planning. The realistic simulator has to contain the real system, the estimator and control algorithms, the environmental model; including disturbances, the magnetic field of the earth, the sun and albedo fluxes; as well as the sensors and actuators. The set of parts modeled have to emulate the whole system well enough to be able to give good estimates of the performance and robustness of the developed estimator and controller algorithms in space [6].

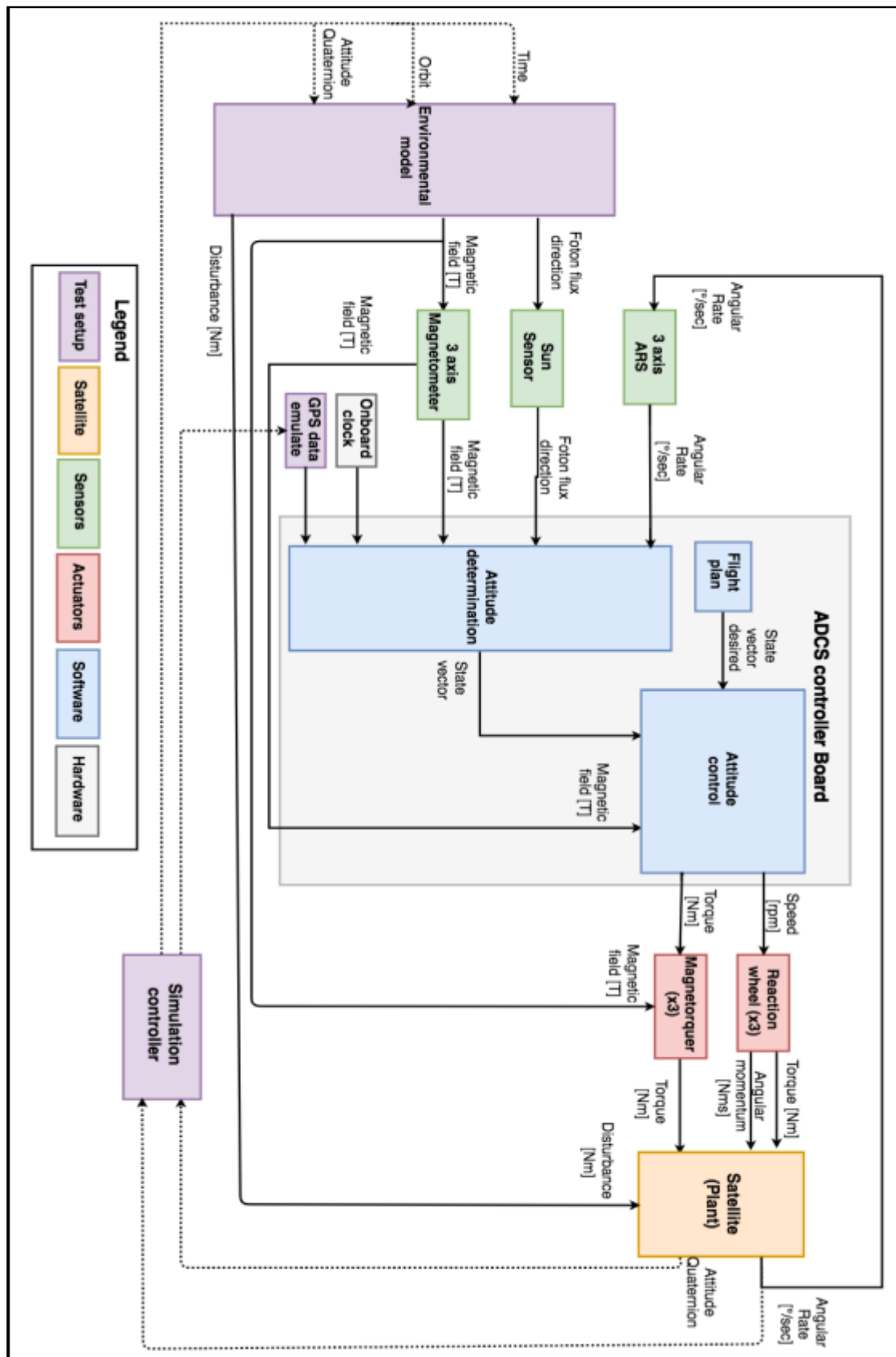


Figure 2-1: Architecture block diagram of an ADCS simulator setup

In Figure 2-1 can identify the different parts or blocks that the ADCS simulation setup has to include and are classified according to if are sensors, actuators, software, hardware, a test setup or the body of the satellite. Each block is defined in terms of input/output and are interconnected as in the real system, next a description of each block is introduced:

- **ARS:** It measures angular velocity. In order to provide angular rate in 3 axes, either one 3-axes MEMS gyro or three 1-axes MEMS gyro are needed.
- **Sun Sensor:** The type of Sun sensor suitable for CubeSat are PSD CMOS. This type of sun sensors measures two angles of the sun light. Three sensors combined will keep the Sun in the FOV during satellite operations.
- **Magnetometer:** It is a sensor that measure the intensity of the magnetic field. The type of sensor suitable for CubeSat are magneto-resistive magnetometer. In order to provide 3 components of the magnetic field, either one 3-axes or three 1-axes Magnetometer are needed.
- **Reaction wheel:** Are actuators that generates torque by accelerating a flywheel mass by a DC motor.
- **Magnetorquer:** Are actuators that generate a magnetic moment. This magnetic moment generated will interact with the Earth magnetic field creating a torque perpendicular to the vector of the magnetic field.
- **GPS data emulate:** It provides orbit information to the attitude determination block
- **Onboard clock:** It provides time information to the attitude determination block.
- **Flight plan:** It represents the information from the Onboard computer with the desired attitude.
- **Simulation controller:** It allows to implement various scenarios of the ADCS and tests for various conditions.
- **Environmental model:** It provides to the ADCS with real values of environmental parameters, such as sunlight, magnetic field or disturbances for the satellite in orbit.
- **Satellite:** This block represents the dynamics of the satellite itself. The inputs are the torques and disturbances applied to the satellite and the angular momentum of the reaction wheels; the outputs are the angular rate of it and its orientation.
- **Attitude determination:** With the sensor data, together with the knowledge of the satellite's position and Sun's position from the ephemerides and the magnetic field model (IGRF) the system reconstructs the satellite's 3-axis attitude. The attitude is obtained differently depending on the satellite is in eclipse or not, Figure 2-2.

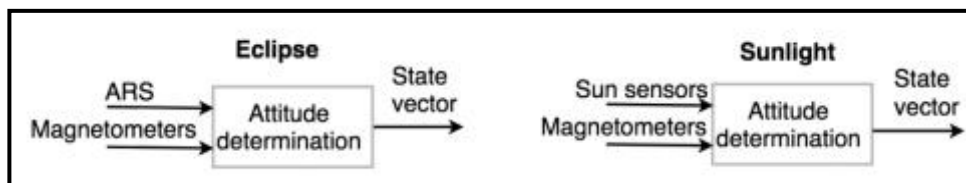


Figure 2-2: Sensors used to obtain the state vector.

- **Attitude control:** It takes the state vector and compared it with the desired state vector. If there is difference between them, the block produces a related control signal to compensate this difference.

## 2.2. Angular rate sensor model

The challenges associated with inertial sensor-based attitude determination for CubeSats is that small-sized sensors that fit within the allowable SWaP constraints tend to have large output errors. Consequently, the attitude solution derived using a gyro only drifts and becomes unusable on short order [2]. In order to establish if the gyro attitude solution can be used in the system and for how long a model has to be developed. Generally, a sensor can be modelled as a black box whose



input is the true measured signal and the output is the estimated measured signal corrupted by errors. The ECSS standard 60-21C, [7], can be applied to the variety of space born gyros, except the gyros used for launch vehicles. It defines the terminology and specifications for the functions and performance of gyros used on spacecraft. Terms used in this thesis about angular rate sensors are derived from the definitions presented in this standard:

- Noise is high frequency or short duration errors
- Angular random walk (ARW) is white noise on the gyro rate output, corresponding to a -1/2 slope on the Allan variance standard deviation plot.
- Rate random walk (RRW): noise component which corresponds to a +1/2 slope on the Allan variance standard deviation plot.
- Bias are gyro measurement errors that are non-stochastic and not input rate dependant, computed as the average of the rate error value over a defined time period.
- Quantisation error is noise due to the digital nature of the gyro output.
- Scale factor error are gyro measurement errors that are non-stochastic and dependant of the rate applied on the input axis.

In the literature, different approaches have been conducted to model the errors that affect the gyros, following different models are presented from the simplest to the most detailed.

A simple model has been developed by Liang Xue, et al [8]. This model only includes bias and ARW. Equation (2-1) states that the angular rate measured is given by the true rate corrupted by ARW,  $\eta_v$ , and bias,  $\beta$ , which is derived from noise RRW,  $\eta_u$ , in equation (2-2).

$$\tilde{\omega}(t) = \omega(t) + \beta(t) + \eta_v(t) \quad (2-1)$$

$$\beta(t) = \int \eta_u(t) \cdot dt \quad (2-2)$$

J. Ambrius and J. Jönsson models a Fibre Optic gyroscope (FOG) as in equation (2-3), in this model two type of bias are defined: Bias stability,  $\beta_s$ , and bias repeatability,  $\beta_R$  [9]. The first is a measurement of how the gyroscope bias drifts over specific time. The second parameter is the error source that creates a constant velocity bias each time the gyroscope is turned on.

$$\tilde{\omega}(t) = \omega(t) + \beta_s(t) + \beta_R(t) + \eta_v(t) \quad (2-3)$$

Liang Xue, Lixin Wang, Tao Xiong, et al. states a general model with the previous error sources along with a scale factor, equation (2-4), [10]. Moreover, Liang Xue specifies that the bias drift is driven by RRW, equation (2-5). They report that, for MEMS ARS with a lower accuracy, the RRW and ARW are considered the most dominant error sources. The ARW is a dominant error in the short cluster time, whereas the bias drift term is the dominant error in the long cluster time.

$$\tilde{\omega}(t) = \omega(t) + S \cdot \omega(t) + \beta_0 + \beta(t) + \eta_u(t) \quad (2-4)$$

$$\beta(t) = \int \eta_u(t) \cdot dt \quad (2-5)$$

The previous gyro models presented differ in the error sources, how they are modeled and which of them are included, but all of them are continuous-time gyro models. In practice, gyroscope gives measurements in discrete-time and therefore it is more suitable to have a discrete-time model, such as the presented by F. Landis and John L in [11]. They derive a discrete-time gyro mathematical model (2-6) and (2-7), from a model equal to [8] by dividing the equation (2-1) by the gyro sampling interval and integrating this equation and equation (2-2).

$$\tilde{\omega}(t) = \omega_{k+1} + \frac{1}{2}(\beta_{k+1} + \beta_k) + \left( \frac{\sigma_v^2}{\Delta t} + \frac{1}{12} \sigma_u^2 \cdot \Delta t \right)^{1/2} N_{vk} \quad (2-6)$$

$$\beta_{k+1} = \beta_k + \sigma_u \cdot \Delta t^{1/2} \cdot N_{uk} \quad (2-7)$$

where the subscript  $k$  denotes the  $k^{\text{th}}$  time-step,  $\sigma_v$  and  $\sigma_u$  are standard deviation of ARW and RRW respectively, and  $N_{vk}$ ,  $N_{uk}$  are zero-mean Gaussian white-noise processes with covariance each given by the identity matrix.

The work presented by F. Landis and John L. in [8] is used as a reference to develop the model of a gyro sensor since is a discrete-time model with the most relevant error sources.

## 2.3. Reaction wheel model

RWs are devices that have to operate continuously in the extreme environment of space. Moreover, the Swap constraints limit the performance of RW in CubeSats. These requirements pose a great challenge to a reaction wheel design, which makes such equipment highly complex and expensive [12]. RWs do not exhibit linear behaviour, the torque of the wheel is not directly proportional to the current applied to the motor [13]. Friction is the major source of the non-linearity in RWs; the friction delays the motor to start till the stator current reaches a certain threshold, introducing a dead zone operation around the zero-speed or when the wheel reverses its rotation sense [14]. For this reason, most of the models that can be found of RW in literature just consider the effect of the friction, as the following examples.

Michael R. Greene models a reaction wheel as a simple rotating mass with inertia  $J_{RW}$  and damping coefficient  $b$  as in equation(2-8), [15].

$$\frac{dh}{dt} = J_{RW} \frac{d\omega}{dt} + b \cdot \omega \quad (2-8)$$

where  $dh/dt$  is the applied wheel torque. It is approximated that all wheel damping is caused by viscous friction,  $b$ .

V. Carrara and H. Kuga present a detailed friction model of a RW, including the viscous friction, Coulomb friction and the friction of Stribeck, equation (2-9), [16].

$$T_{RW} = J_{RW} \frac{d\omega}{dt} + b \cdot \omega + \text{sgn}(\omega) \left[ c + d \cdot e^{-\frac{\omega^2}{\omega_s^2}} \right] \quad (2-9)$$

where  $T_w$  is the motor torque, the wheel's and rotor inertia is  $J_{RW}$ ,  $b$  is the coefficient of viscous friction,  $c$  is the Coulomb friction torque,  $d$  is the starting torque,  $\omega$  is the angular velocity of the wheel and  $\omega_s$  is known as Stribeck speed. They display the torque model graphically in Figure 2-3.

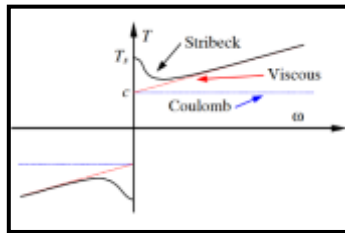


Figure 2-3: Friction torque model used in [16]

In addition to friction, other elements also affect the behaviour of the RWs. The DC electric motor commonly used in reaction wheels are permanent magnet alternating current (PMAC) motors. PMAC motors are a type of a DC motor whose commutation is done electronically instead of using brushes. By cause of this commutation, there may be a ripple in the torque, if this ripple is considerable, the RW may affect in some degree the stability of the satellite. Figure 2-4 shows torque with ripple generated by a PMAC motor.

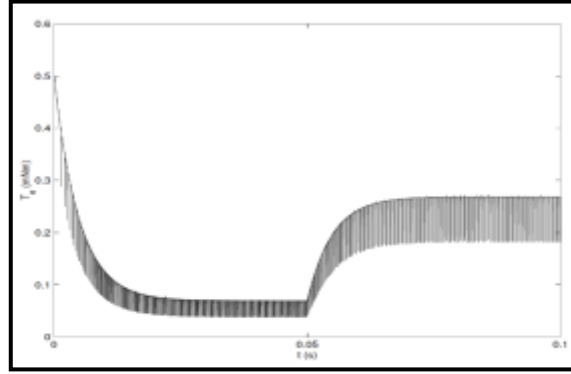


Figure 2-4: Torque ripple generated by PMAC motor [17]

Reaction wheels can be controlled with speed control or torque control. In torque control, since the current is proportional to torque, the electronics deliver the necessary current to the motor in order to achieve the commanded torque. Contrarily, speed control has a cascade control where the outer loop keeps the speed as desired and an inner loop controls the current. Figure 2-5 shows a Speed control configuration. Speed control without cascade control can have bigger torque ripple, and the current can get larger and burn the power electronics and the motor [18].

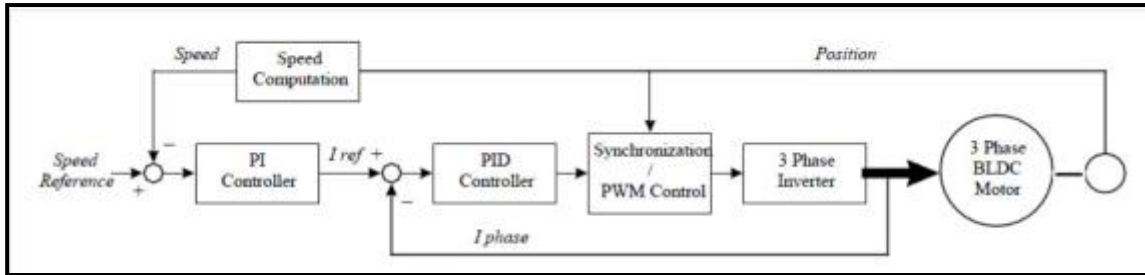


Figure 2-5: Speed control configuration for a BLDC motor [19]

Ø. Andresen, et al, describe a simplified model with speed control, implemented in Simulink Figure 2-6, [20]. In this case, the RW has an internal closed-loop discrete PID controller that keep the velocity at the desired value. Andresen's model is linearized, and it can only be used around a bias point, never reaching zero or negative voltages in operation. Further, the commutation effect is not represented in his model. The Dc motor of the RW is modelled as in equation (2-10), which relates the armature voltage,  $v$ , with the armature current,  $i$ , and the angular velocity of the motor  $\omega$ .

$$v = R \cdot i + L \frac{di}{dt} + K_S \cdot \omega \quad (2-10)$$

where  $R$  is the resistance of the stator,  $L$  the inductance of the stator, and  $K_S \omega$  is the electromotive force produced when a conductor is moved in a magnetic field. The torque of the reaction wheel is presented in equation (2-11), which states that the torque,  $T_{RW}$ , is proportional to the torque produced by the motor,  $kt \cdot i$ , and the torque generated by friction.

$$T_{RW} = J_{RW} \frac{d\omega}{dt} = k_t \cdot i + b \cdot \omega \quad (2-11)$$

where  $b$  is the viscous friction coefficient,  $k_t$  is the motor torque constant and  $J_{RW}$  is the moment of inertia of the reaction wheel.

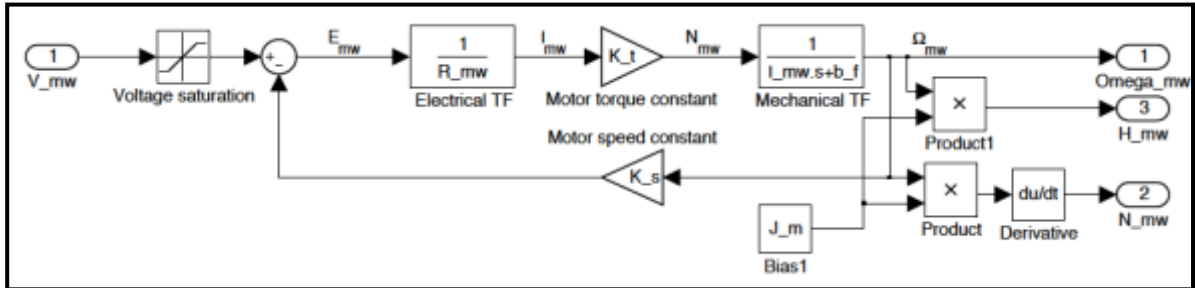


Figure 2-6: Simulink implementation of a RW model [20]

PMAC motors are classified mainly into two types namely Permanent Magnet Synchronous Motor (PMSM) and Brushless Direct Current Motor (BLDCM) [21]. The stator winding of BLDCM Motor is concentrated Figure 2-7 left, generating a trapezoidal shape back electromotive force (EMF) waveform Figure 2-8. Whereas in PMSM the stator winding is distributed Figure 2-7 right, and the motor generates a sinusoidal back EMF Figure 2-9. The back EMF is the voltage caused by the relative motion between the stator and the rotor, which opposes the main voltage supplied to the winding according to Lenz's law [22].

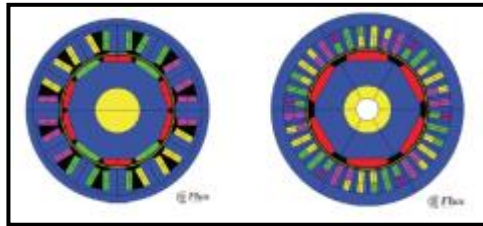


Figure 2-7: PMAC motor with concentrated winding (left) and with distributed winding (right) [23].

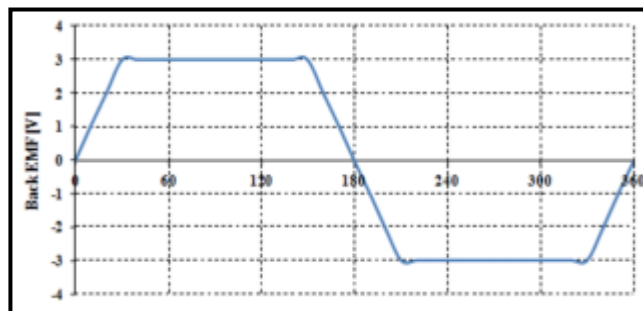


Figure 2-8: Trapezoidal Back EMF from BLDCM [24].

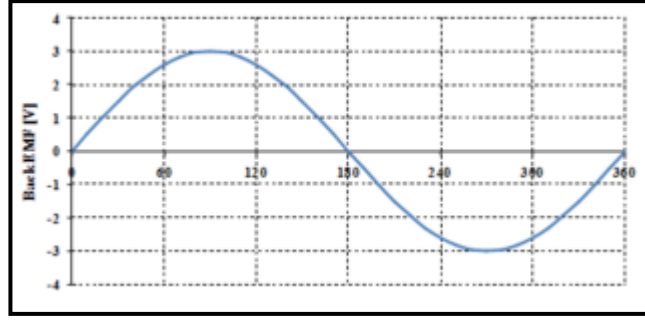


Figure 2-9: Sinusoidal Back EMF from PMSM [24].

It can be found three commonly used commutation methods to control the rotation on PMAC motors: trapezoidal (six step), sinusoidal and field oriented control (or vector control). In order to get minimum torque ripple, trapezoidal commutation is used with BLDC motors and sinusoidal with PMS motors. However, these right combinations still have drawbacks: the trapezoidal commutation generates torque ripple, and sinusoidal is inefficient at high speeds [25]. The FOC can apply to both types of motors to get the best drive performances giving smooth operation at low speed and efficient running at high speed, but it may require extra code development and hardware components [25]. RW models that include the commutation effects have a high frequency setup, thus their simulations are slow.

In this thesis, only RWs with BLDC motors, trapezoidal commutation, and speed control are explored. The controller with trapezoidal commutation activates the phases in a predetermined sequence determined by the position of the rotor. The rotor position information is only need within 60-degree sector; therefore, low-cost Hall-effect sensors are usually used [26]. Besides, the speed information can be estimated using the Hall effect sensors by timing their generated pulses [26].

Previous models commented doesn't represent well enough the behaviour of RW. Differently the model presented by Ricardo Pereira in [27] includes the effects of friction and commutations. He develops an accurate model of a three-phase BLDC motor with trapezoidal commutation to design and develop a reaction wheel. However, this model does not include a speed control of the RW, but it is open loop. This model assumes that:

- Magnetic circuit saturation is ignored;
- Stator resistance, self and mutual inductance of all phases are equal and constant;
- Hysteresis and eddy current losses are eliminated;
- All semiconductor switches are ideal and no losses are going to be considered;

He expresses the voltage equation of a BLDC as equation (2-12).

$$\begin{aligned} V_a &= R_a + L \frac{di_a}{dt} + E_a \\ V_b &= R_b + L \frac{di_b}{dt} + E_b \\ V_c &= R_c + L \frac{di_c}{dt} + E_c \end{aligned} \quad (2-12)$$

where  $L$  is the armature self-inductance;  $R$  is the armature terminal resistance;  $V_a, V_b, V_c$  are the terminal phase voltage;  $i_a, i_b, i_c$  are the motor input current; and  $E_a, E_b, E_c$  are the back-EMF voltage of the motor for each phase. Ricardo uses a back-EMF approximated to ideal trapezoidal waveform as a function of the rotor position and the back-EMF of each phase has 120° phase angle, equation (2-13).

$$\begin{aligned}
 E_a &= k_\omega \cdot f(\theta_e) \cdot \omega \\
 E_b &= k_\omega \cdot f\left(\theta_e - \frac{2\pi}{3}\right) \cdot \omega \\
 E_c &= k_\omega \cdot f\left(\theta_e + \frac{2\pi}{3}\right) \cdot \omega
 \end{aligned} \tag{2-13}$$

Where  $k_\omega$  is the back-EMF constant [V/rad/s] and  $\theta_e$  is the electrical angle related to the rotor or mechanical angle,  $\theta_m$  by the number of poles of the motor as in equation (2-14).

$$\theta_e = \frac{P}{2} \theta_m \tag{2-14}$$

Moreover, the  $f(\theta_e)$ , which is the back-EMF reference function which has trapezoidal shape and maximum magnitude of 1, can be represented by equation (2-15).

$$f(\theta_e) = \begin{cases} 1, & \text{if } 0 \leq \theta_e \leq 2\pi/3 \\ 1 - \frac{6}{\pi}(\theta_e - 2\pi/3), & \text{if } 2\pi/3 \leq \theta_e \leq \pi \\ -1, & \text{if } \pi \leq \theta_e \leq 5\pi/3 \\ -1 + \frac{6}{\pi}(\theta_e + 5\pi/3), & \text{if } 5\pi/3 \leq \theta_e \leq 2\pi \end{cases} \tag{2-15}$$

The total electromagnetic torque (2-17) can be represented as the summation of the electromagnetic torque of each phase equation (2-16),

$$\begin{aligned}
 T_a &= k_\omega \cdot i_a \cdot f(\theta_e) \\
 T_b &= k_\omega \cdot i_b \cdot f(\theta_e - 2\pi/3) \\
 T_c &= k_\omega \cdot i_c \cdot f(\theta_e + 2\pi/3)
 \end{aligned} \tag{2-16}$$

$$T_e = T_a + T_b + T_c \tag{2-17}$$

At last, the mechanical torque provided by the RW is expressed by the equation (2-18),

$$T_{RW} = T_e - T_i = J_{RW} \frac{d\omega}{dt} + b \cdot \omega \tag{2-18}$$

where  $T_i$  is the load torque and  $b$  is the dynamic friction torque constant.

The model that represents the RW well enough is a slow model, due to the commutations, invalidating its use in the ADCS simulator, the other models that are faster don't represent the commutation effect on the torque. Thus, it is clear that is not possible to develop a model suitable for the ADCS simulator and able to show torque ripple and realistic transient response at the same time. Consequently, two models of RW are developed, one simplified for the ADCS simulator and one to study the torque ripple and transient response. The model presented by Ricardo in [27] is used as a reference to develop a detailed model of a reaction wheel, though it is necessary to integrate a speed controller. As for the simplified model, the friction model presented by Michael R. Greene in [15] is used as a source to develop a numerical model to use in the ADCS simulator.

## CHAPTER 3

# Implementing mathematical models

### 3.1. Implementing angular rate sensor model

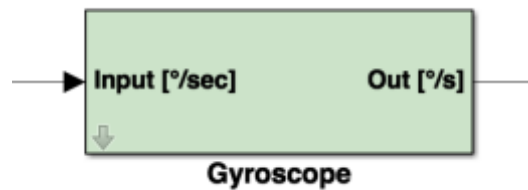


Figure 3-1: Black box model gyroscope

The ADIS16135 sensor is used as a reference during the development of the model of a gyroscope. It is a high performance, digital gyroscope sensing system and its datasheet contains all the crucial information to develop an accurate model. The mathematical model defines a 1-axis gyroscope as a black box model, Figure 3-1, whose input is the real angular rate and the output is the estimated angular velocity. The model has been divided into different modules that forms the different parts of the sensor signal chain Figure 3-2:

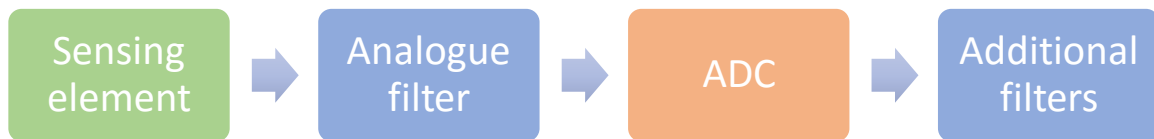


Figure 3-2: Sensor signal chain modules

#### 3.1.1. Sensing element model

The opening and most important module is the sensing element, which converts the real angular rate into a representative electrical signal corrupted by errors. The model developed is focused on the possible behaviour of the sensor in orbit. Accordingly, the model includes the most dominant error sources that the sensor in orbit conditions will be subjected, i.e. RRW, ARW and nonlinearity scale factor. However, this model does not comprise other noise that may have a minor influence on the response of the sensor, such as the following:

- The changes in temperature in the sensor introduce an error. Nonetheless, gyroscopes usually are assembly together with a temperature sensor making possible to compensate the error of temperature changes. In this model, it has been assumed that the temperature compensator is annulling the temperature error.
- Whenever the sensor is turned on, there is an offset, known as bias repeatability. This bias error component may be different every time is turn on as a result of relaxation of the mass in the spring system, temperature distribution that is not yet homogeneous during the warm-up phase [28]... This error is assumed that is estimated and compensated during sensor calibration.
- Mechanical imperfections when gyroscopes are installed onto the platform causes misalignment errors as a result of misalignment between the sensor's axis of rotation and

the system's reference frame [29]. In this model, it has been considered the axis of the sensor and the system reference frame ideally aligned.

- The bias voltage sensitivity is the error caused by the change in the supply voltage of the sensor. This change is due to a small unwanted periodic variation voltage in the dc-dc converter, known as ripple. It is expected that the error caused by the ripple is lower than the sensitivity of the sensor, and thus this error is insignificant.
- Linear motion or vibrations on the sensor cause a bias error on the measurements. However, the satellite is on a high enough orbit, has not thrusters and the RWs are not powerful enough to cause significant vibration on the sensor board; hence this error can be assumed insignificant.
- Since this model only covers 1-axis gyroscopes the cross-axis coupling factor, i.e. the error induced by the application of angular rate on a perpendicular axis, has not been studied.

Following on the definitions in 2.2 and base on the model presented by F. Landis and John L. in [10], the core sensor element model has been developed, equations (3-1) and (3-2).

$$\tilde{\omega}(t) = (1 + NL) \cdot \omega_{k+1} + \frac{1}{2} (\beta_{k+1} + \beta_k) + \left( \sigma_v^2 \cdot F_s + \frac{1}{12} \sigma_u^2 \cdot \left( \frac{1}{F_s} \right) \right)^{1/2} N_{vk} \quad (3-1)$$

$$\beta_{k+1} = \beta_k + \sigma_u \cdot \left( \frac{1}{F_s} \right)^{1/2} \cdot N_{uk} \quad (3-2)$$

### 3.1.2. Analogue filter model

The core element sensor is followed by a signal-conditioning circuit, which is an analogue filter designed in continuous time (s) as a 2-pole ( $\omega_1$  and  $\omega_2$ ) low-pass filter, equation (3-3). However, since the gyro model is discrete, the filter is modeled as an equivalent discrete-time filter (z) that represents a real continuous time filter with step time given by the bandwidth of the sensor. Equation (3-4) shows the z-transform function of the filter for the ADIS16135 sensor obtained from equation (3-3) using Tustin approximation [30].

$$H_G(s) = \frac{\omega_1}{s + \omega_1} \cdot \frac{\omega_2}{s + \omega_2} \quad (3-3)$$

$$H_G(Z) = \frac{0.8396z + 0.06947}{z^2 - 0.09155z + 0.0005575} \quad (3-4)$$

### 3.1.3. Analogue to digital converter model

The gyroscopes include an Analogue to Digital Converter (ADC) to transform the signal from analogue domain in the digital domain. The conversion process includes three operations:

- Sampling: Converts a continuous signal on time to a discrete signal on time, in this model since it is discretised, the signal only is sampled at other sampling time.
- Quantization: Converts a continuous signal on amplitude to a discrete signal on amplitude. It is in this phase where the quantization error is produced due to the rounding process
- Coding: Converts a decimal signal to a binary signal. This part is not included in the model.



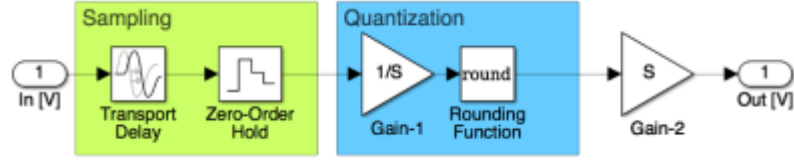


Figure 3-3: ADC Simulink model

Figure 3-3 is the ADC model implemented in Simulink. The sampling operation model includes a delay block that represents the time needed to realize the ADC process and it's equal to the sampling period of the ADC. And a zero-order hold which samples the signal and holds the value until the next sample. The quantization process is modeled with a gain block and a rounding function block. The former scales the signal within the range of the total bits of the sensor and next is rounded to the nearest integer value. The model includes a second gain model needed to rebuild the signal in analogue value for simulations. The ADC model does not include instabilities in the ADC's clock.

### 3.1.4. Additional filters model

The ADIS16135 sensor also incorporates digital and decimation filters. First there are two consecutive  $N_F$ -order Finite Impulse Response (FIR) averaging filters. The output of an averaging filter is the arithmetic mean of the current and previous inputs, the impulse response of this filter is of finite duration [31]. The order of a digital filter is the number of previous inputs used to calculate the current output, and it can be set with different values with a register in the sensor. The default register defines a 15-order filter, the transfer function of one of the filters is obtained by the Z-transform in equation (3-5).

$$\frac{y_n}{x_n} = \frac{1 + z^{-1} + z^{-2} + \dots + z^{-15}}{16} \quad (3-5)$$

Followed it has an averaging/decimation filter formed by decimation filter that samples the signal at low rate with a decimation factor  $N_{DF}$ , which is set with a register on the sensor, and by  $(N_{DF}-1)$ -order FIR averaging filter. The decimation factor is the ratio of the input rate to the output rate, equation (3-6).

$$N_{df} = \frac{\text{Input rate}}{\text{Output rate}} \quad (3-6)$$

## 3.2. Implementing reaction wheel models

Figure 3-4 shows the black box view for the RW models. Its input is the desired speed, and its outputs are the real speed, the torque and the angular momentum.

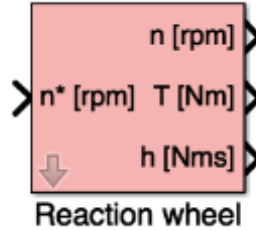


Figure 3-4: Black box of reaction wheel model

### 3.2.1. “Open loop” model of RW.

An “open loop” model is used as a first step to develop a detailed model of a reaction wheel. The open-loop model is derived directly from the model presented by Ricardo and described in section 2.3. The open loop model can be used to verify the behaviour of the BLDC motor model and investigate the maximum speed for the parameters used. As indicates its name, this mode has not speed or torque control; it accelerates until reaches maximum speed.

Besides the assumption presented in 2.3, the assumptions adopted in the development of the model are:

- Back EMF has ideal trapezoidal shape. The model of back-EMF approximated to ideal trapezoidal waveform in BLDC motor system has generally been used in computer simulation tools [32]. The real shape of the back-EMF waveform of BLDC is shown in Figure 3-5.

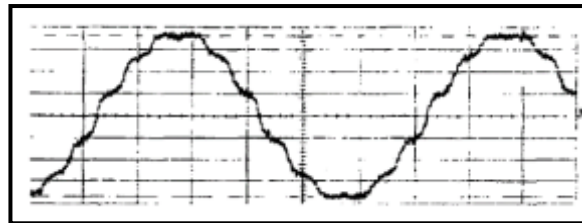


Figure 3-5: measured real back EMF waveform of BLDC motor [48].

- It has been assumed that each phase current is independent. For simplicity of the model, the current of each phase is independent when in reality the same current pass through the two active phases.
- RW is assumed aligned with respect to the Satellite principal axes [27].
- Feedback sensors of the reaction wheel are assumed ideal, the models of the sensors are modelled without any error source or noise. Besides, the hall sensors are assumed that provide a continuous signal.
- The back current produced by the back EMF is dissipated on a resistive load. It has been assumed that there is no phase current when no voltage is applied to the respective phase.
- Only viscous friction is included in the model. The Coulomb friction and the friction of Stribeck are assumed negligible.

The model is divided into various blocks which represent the different parts that make up the reaction wheel, Figure 3-6, a BLDCM with flywheel, a 3-phase inverter, a hall sensors and a commutation blocks; following these blocks are explained.

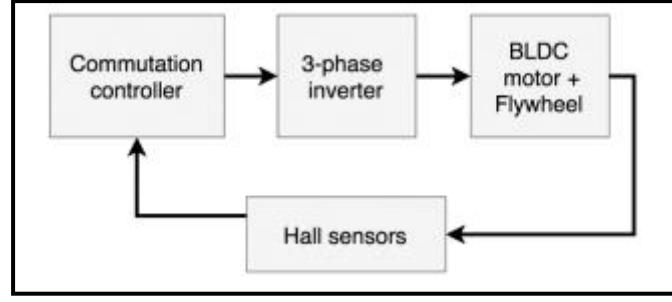


Figure 3-6: Architecture "Open loop" model of reaction wheel

#### 3.2.1.1. BLDC motor & flywheel block

This block represents the BLDC motor coupled with the flywheel. It is modelled as Ricardo in [27], detailed in chapter 2.3, with equations (2-12), (2-13), (2-14), (2-15), (2-16), (2-17) and (2-18).

#### 3.2.1.2. Hall Sensors block

Three hall effect sensors mounted on the motor shaft are commonly used for sensing the rotor position of a BLDC motors [22]. The Hall effect sensors employed in BLDC motors give a high signal when the magnetic poles of the rotor pass near the sensor. By combining the signals from the three sensors, the position of the rotor is determined. The three Hall sensors are modelled as equation (3-7), where  $\theta_e$  is the electrical angle obtained from the rotor angle from equation (2-14).

$$\begin{aligned}
 Hall_A &= 1, \quad \text{if} \quad 0 \leq \theta_e \leq \pi \\
 Hall_B &= 1, \quad \text{if} \quad \frac{2}{3}\pi \leq \theta_e \leq \frac{5}{3}\pi \\
 Hall_C &= 1, \quad \text{if} \quad \frac{4}{3}\pi \leq \theta_e \leq \frac{1}{3}\pi
 \end{aligned} \tag{3-7}$$

#### 3.2.1.3. 3-phase inverter circuit block

The 3-phase inverter is an electronic circuit that drives the BLDC motor by commutating the DC supply voltage to the three phases of the motor. The three-phase inverter has six power switches, two on each phase leg which are connected to the DC voltage source. Figure 3-7 shows a three-phase full-bridge inverter. By activating a positive and a negative switch in two phase legs, the current flows through the transistor which conducts positive, pass through two phases of the BLDC motor and returns through the negative transistor. The switches are activated by the control signals (Q1, Q2, Q3, Q4, Q5, Q6) from the commutation controller.

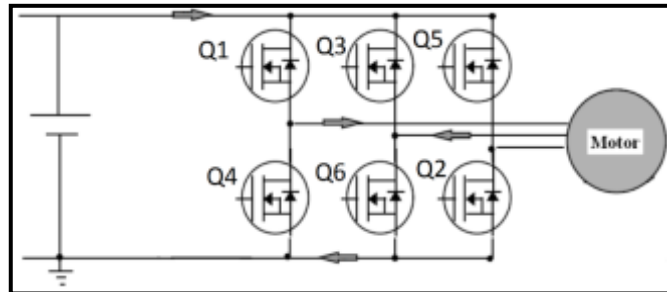


Figure 3-7: 3-phase inverter circuit

The Inverter circuit is modeled as in Equation (3-8).

$$\begin{aligned}
V_A &= V_{CC} \cdot Q1 - V_{cc} \cdot Q4 \\
V_B &= V_{CC} \cdot Q3 - V_{cc} \cdot Q6 \\
V_C &= V_{CC} \cdot Q5 - V_{cc} \cdot Q2
\end{aligned}
\tag{3-8}$$

### 3.2.1.4. Commutation controller block

The six inverter switches have to be activated with a particular sequence to get clockwise or counter-clockwise rotation. This sequence depends on the position of the rotor obtained from the information of the hall sensors, by choosing the right phase pair in each rotor position the motor can produce the highest torque. The activation sequence for clockwise rotation as a function of the rotor position and the hall sensor information is shown in Table 1 and Table 2 for counter-clockwise rotation. By energizing each phase when the back EMF is maximum, theoretically makes possible to produce a constant torque. In practice, the current is not established instantaneously in a motor phase due to the inductances, as a consequence torque ripple is produced every time there is a phase commutation [25].

Table 1: Clockwise rotation switches sequence

Electrical angle	A hall	B hall	C hall	Q1	Q4	Q3	Q6	Q5	Q2
0-60	1	0	1	1	0	0	1	0	0
60-120	1	0	0	1	0	0	0	0	1
120-180	1	1	0	0	0	1	0	0	1
180-240	0	1	0	0	1	1	0	0	0
240-300	0	1	1	0	1	0	0	1	0
300-360	0	0	1	0	0	0	1	1	0

Table 2: Counter-clockwise rotation switches sequence

Electrical angle	A hall	B hall	C hall	Q1	Q4	Q3	Q6	Q5	Q2
0-60	1	0	1	0	1	1	0	0	0
60-120	1	0	0	0	1	0	0	1	0
120-180	1	1	0	0	0	0	1	1	0
180-240	0	1	0	1	0	0	1	0	0
240-300	0	1	1	1	0	0	0	0	1
300-360	0	0	1	0	0	1	0	0	1

### 3.2.2. Speed control model

To have the RW rotating at the desired velocity a cascaded speed control is added to the previous model, Figure 3-8. It uses the Pulse Width Modulation (PWM) technique that adjusts the duty cycle of a pulse to control the electrical power applied to analogue circuits such as electric motors based on the information from controllers [33]. Thus, the inverter switches are active following the previous sequence, section 3.2.1.4, and at the same time following the PWM signal of the controller. There are two ways of handling the switching of the transistors: hard-chopping and soft-chopping. In the hard-chopping both phase transistors are driven by the same pulsed signal: the two transistors are switched-on and switched-off at the same time. In the soft-chopping, the low side transistor is left ON during the phase supply and the high side transistor switches according to the pulsed signal [19]. In the model a hard-chopping technique is used to switch the transistors, but with each transistor signal independent.

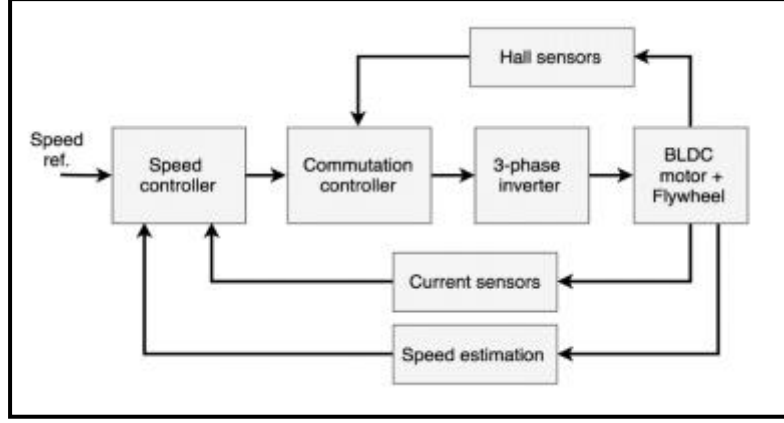


Figure 3-8: Architecture Speed control model of reaction wheel

Figure 3-9 shows the design of the speed controller. The desired and the actual speed are compared, and a respective error signal is put into a PI controller giving a desired current signal which is compared with the real current to provide the duty cycle value.

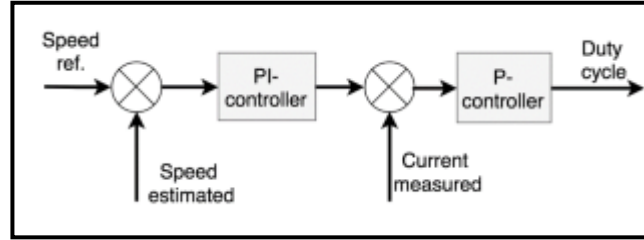


Figure 3-9: Speed controller configuration

It is important when designing a cascade controller for a BLDC motors that the inner controller is around 4-5 times faster (higher bandwidth) than the outer controller or the system can become unstable [65]. The speed sensor is modeled as a zero-order hold with sampling frequency 1000 Hz. The current sensor is modeled as in equation (3-9) with a zero-order hold with a frequency of 5000Hz.

$$I_{estimated} = \frac{1}{2} \sum_{i=1}^n I_i, \quad i = A, B, C \quad (3-9)$$

### 3.2.3. Simplified reaction wheel model

A simplified model of a reaction wheel with speed control is developed to be simulated with the ADCS simulator. This model, however, does not include commutation effects and only involve viscous friction. Following equations describe the simplified model, equation (3-10) states that the torque of the RW is given by the difference between the commanded speed,  $n^*$ , and the actual speed,  $n$ , by the winding coefficient,  $k$ , minus the torque friction,  $T_f$ . As Michael R. Greene model in [15], the friction torque is approximated by only viscous friction. The angular speed of the RW, equation (3-11), is obtained by the integration of the division of the torque and the moment of inertia of the RW,  $J$ . The angular momentum of the wheel is equal the moment of inertia by the angular speed, equation (3-12).

$$T_{RW} = (n^* - n)k - T_f \quad (3-10)$$

$$n = \frac{1}{s} \left( \frac{T_{RW}}{J} \right) \quad (3-11)$$

$$h = J \cdot n \quad (3-12)$$

### 3.3. Implementing satellite dynamic model

To verify the behaviour that the RWs produce to the satellite, a model of the dynamics of the satellite is also developed. Figure 3-10 shows the black box model of the satellite with inputs of the torque and angular momentum from the reaction wheels and external torque. Its outputs are the angular momentum, the angular velocity and the attitude in a quaternion form, in Appendix B the derivation of the quaternion from the angular speed is described.

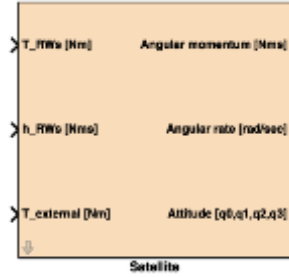


Figure 3-10: Satellite dynamics black box model

Spacecraft attitude changes according to the fundamental equations of motion for rotational dynamics, the Euler equations, here expressed in vector form in the spacecraft's reference frame, equation (3-13) [5]. The second term of the equation is only present when the satellite has angular speed or angular momentum.

$$\frac{d\vec{H}}{dt} = \vec{T} - \vec{\Omega} \times \vec{H} \quad (3-13)$$

where  $T$  is torque,  $\Omega$  is the angular velocity of the satellite and  $H$  is the angular momentum, that is the rotational motion of a body that will continue unless changed by a torque, eq. (3-14).

$$\vec{H} = J_B \cdot \vec{\Omega} \quad (3-14)$$

$J_B$  is the moment of inertia, a 3-by-3 matrix of values that describe the distribution of mass in a body. There is always a coordinate frame, called the principal axis frame<sup>1</sup>, for which the moment of inertia matrix is diagonal. Note that in (3-13), it is clear that the magnitude of angular momentum in a system can only be changed by applying external torques,  $T$ , because the change due to  $\Omega \times H$  term can only alter the direction of  $H$ , not the magnitude. This effect is known as the gyroscopic stiffness; and it is the phenomena whereby the spin axis of a freely rotating body keeps its orientation fixed in inertial space and resists any attempt to change. The gyroscopic stiffness is proportional to the moment of inertia  $J_B$  of the body around its spin axis, as well as to the spin rate  $\Omega$ . If we want to force the body to change its orientation, we must apply a torque  $T$ .

Although some spacecraft can be modelled as a single rigid body, equation (3-13), many are more complex. If we consider a satellite with  $n$  reaction wheels or control moment gyros, labelled by an index  $i$ . Each wheel rotates about its spin axis with angular velocity  $\omega_i^w$  with respect to the body. The wheel is axially symmetric about its spin axis, so the spin axis is a principal axis with principal moment of inertia  $J_i^{\parallel}$ , and every axis perpendicular to the spin axis is a principal axis with moment of inertia  $J_i^{\perp}$ . Thus, the inertia tensor of the  $i$ th wheel in the body reference frame is expressed in equation (3-15).

<sup>1</sup> Assuming that COG is close to the geometrical center and the shape of the satellite is symmetrical, the principal axis frame can be considered coincident with the body frame.

$$J_i^w = J_i^\perp (I_3 - \hat{w}_i \hat{w}_i^T) + J_i^\parallel \hat{w}_i \hat{w}_i^T \quad (3-15)$$

where the unit vector  $\hat{w}_i$  defines the spin axis in the body frame.  $I_3$  is the identity matrix. Letting  $\tilde{J}_B$  represent the moment of inertia of the spacecraft without the wheels, the body frame representation of total angular momentum with respect to inertial space of the spacecraft with its wheels is defined in equation (3-16) [11].

$$\vec{H} = J_B \cdot \vec{\Omega} + \vec{h} \quad (3-16)$$

where  $J_B$  is the body moment of inertia including the inertia of the wheels transverse to their spin axes, but not their inertia along their spin axes (3-17).

$$J_B \equiv \tilde{J}_B + \sum_{i=1}^n J_i^\perp (I_3 - \hat{w}_i \hat{w}_i^T) \quad (3-17)$$

In the case of a 3-reaction wheel,  $J_i^\perp$  is 0 or near 0, therefore  $J_B \approx \tilde{J}_B$ . And where  $\vec{h}$  denotes only the angular momentum of the wheels along their spin axes.

$$\vec{h} = \sum_{i=1}^n h_i \hat{w}_i \quad (3-18)$$

The derivate of equation (3-16) gives equation (3-19)

$$\frac{d\vec{H}}{dt} = J_B \cdot \frac{d\vec{\Omega}}{dt} + \frac{dJ_B}{dt} \cdot \vec{\Omega} + \frac{d\vec{h}}{dt} \quad (3-19)$$

substituting H in the equation (3-13) and using equations (3-19) and (3-16)

$$J_B \cdot \frac{d\vec{\Omega}}{dt} + \frac{dJ_B}{dt} \cdot \vec{\Omega} + \frac{d\vec{h}}{dt} = \vec{T} - [\vec{\Omega} \times (J_B \vec{\Omega} + \vec{h})] \quad (3-20)$$

after moving some parts equation (3-21) is obtained which describes the dynamics of a satellite with reaction wheels.

$$J_B \cdot \frac{d\vec{\Omega}}{dt} + \frac{dJ_B}{dt} \cdot \vec{\Omega} = \vec{T} - \frac{d\vec{h}}{dt} - [\vec{\Omega} \times (J_B \vec{\Omega} + \vec{h})] \quad (3-21)$$

where:

- The term  $\frac{dJ_B}{dt} \cdot \vec{\Omega}$  shows how changes in the spacecraft moment of inertia, such as by solar array articulation, can affect attitude dynamics.
- The term  $\vec{T}$  represents the torque's direct contribution to attitude dynamics; this term includes how some actuators, magnetorquers for the case of R-3A, can be used to control spacecraft attitude by creating torques.
- The term  $\frac{d\vec{h}}{dt}$  gives the relationship between changes in on-board rotating objects' speeds and changes in the spacecraft's rotational velocity; this term is where certain other control actuators enter into the dynamics as so-called internal torques.
- The term  $[\vec{\Omega} \times (J_B \vec{\Omega} + \vec{h})]$  is called the **gyroscopic torque**, and it shows how the angular momentum appears to change direction, but not magnitude, in the spacecraft's frame of reference when the spacecraft is rotating.

Lastly, during a normal lifetime of the satellite, it is considered that there are no changes in mass properties, consequently, the term  $\frac{dJ_B}{dt} \cdot \vec{\Omega}$  disappears getting the equation (3-22), which is used to implement the satellite dynamics model.

$$J_B \cdot \frac{d\vec{\Omega}}{dt} = \vec{T} - \frac{d\vec{h}}{dt} - \left[ \vec{\Omega} \times (J_B \vec{\Omega} + \vec{h}) \right] \quad (3-22)$$



## CHAPTER 4

# Simulations based on models

## 4.1. Angular rate sensor simulations

### 4.1.1. Model parametrization

As said in section 3.1, the sensor ADIS16135 is used to develop the model, additionally the Gypro2300 and CRM200 sensors are also simulated. Their parameters can be found in Table 3.

Table 3: Gyroscopes parameters used in the mathematical model

Parameter	Symbol	ADIS16135	Gypro2300	CRM200
Dynamic range [°/s]	DR	300	300	75
Bandwidth [Hz] <sup>2</sup>	B	335	100	50
Data rate [Hz]	F <sub>s</sub>	1024	200	100
Sensitivity [°/sec/LSB]	S	0.0125	0.1 · 10 <sup>-3</sup>	0.0104
Rate Noise Density [°/sec/√Hz rms]	σ <sub>v</sub>	0.0122	0.00399	0.018
Bias stability [°/sec]	Bias	0.0017	0.00022	0.0066
Nonlinearity [% DR]	NL	±0.008	±0.05	±0.06
Coefficient FIR filter	N <sub>F</sub>	16	Non-filter	Non-filter
Decimation factor	N <sub>DF</sub>	16	Non-filter	Non-filter

The dynamic range is the range over which the sensor can measure angular rate. The bandwidth is the passband frequencies defined by the analogue filter. The data rate is the frequency that the sensor updates the signal, in those sensors this parameter can be varied, however, in Table 3 there is the default data rate value specified on the datasheets. The most common metrics that MEMS gyroscope datasheets offer to describe their noise behaviours are Rate Noise Density (RND) and angle random walk (ARW) [34]. The RND parameter describes the gyro's inherent noise for a particular filter configuration; differently, the ARW parameter is often more useful when analysing the impact that noise has on angle estimation over specific periods of time. In this model, the RND parameter is used to parametrize the standard deviation of ARW noise. The standard deviation of the RRW is parametrized by bias stability parameter over the data rate of the sensor, equation (4-1).

$$\sigma_u = \frac{Bias}{\sqrt{F_s}} \quad (4-1)$$

Nonlinearity is the maximum deviation of the output from the expected value using a best fit straight line. The coefficient of the FIR filter is the order of the filter plus 1.

### 4.1.2. Verification model

Allan variance is a time domain analysis technique that is applied to analyse the error characteristics of any precision measurement instrument, it is described in APPENDIX A. Many sensor's manufacturers provide the Allan variance of the real sensor, thus making possible a comparison with the Allan variance of the model and giving a tool to verify the appropriateness

<sup>2</sup> This parameter cannot be changed by block parameters

of the model. The model has been proved with ADIS16135 and GYPRO2300, Figure 4-1. The Allan variance is simulated over 5.5 hours for a zero-rate input with an averaging time range from 1 sec to 1000 sec without additional filters block.

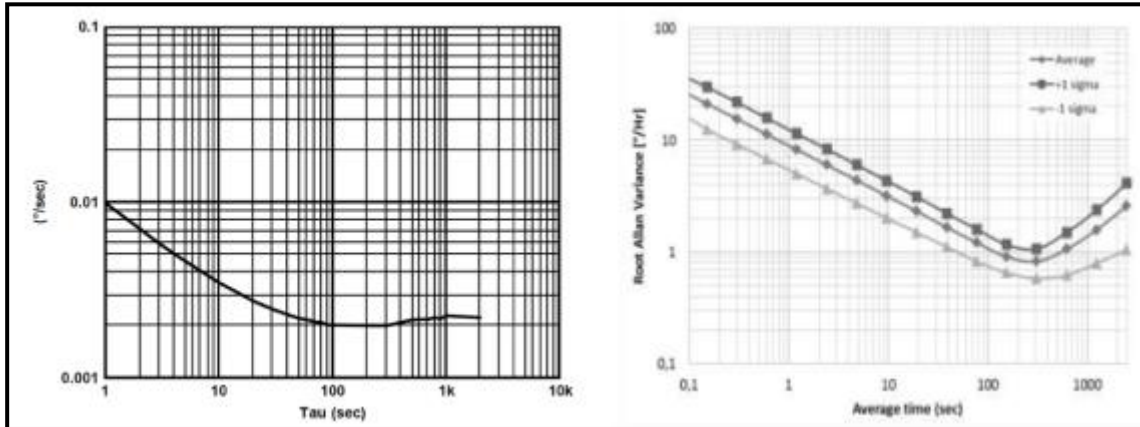


Figure 4-1: Allan variance datasheets ADIS16135 (left) Gypro2300 (right)

Figure 4-2 shows the model's Allan variance plot with parameters of ADIS16135 and the curve from the datasheet sensor. Figure 4-3 presents the results of the model for the GYPRO's parameters and the average curve from the GYPRO sensor datasheet.

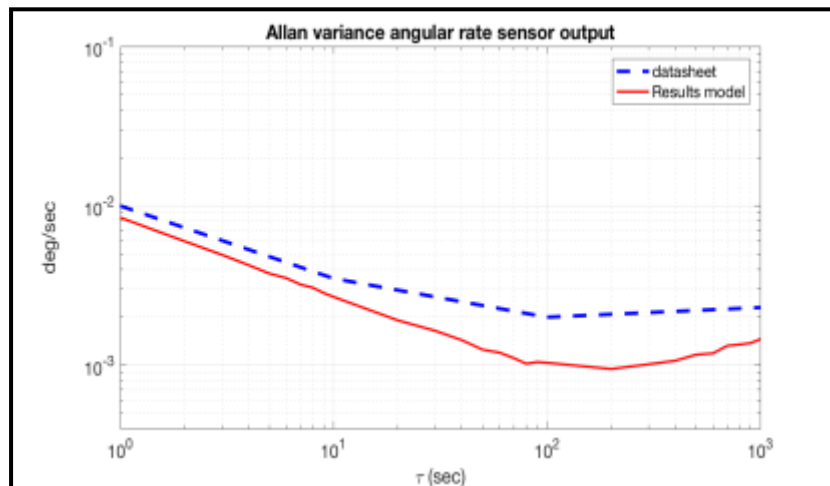


Figure 4-2: Allan variance model ADIS16135

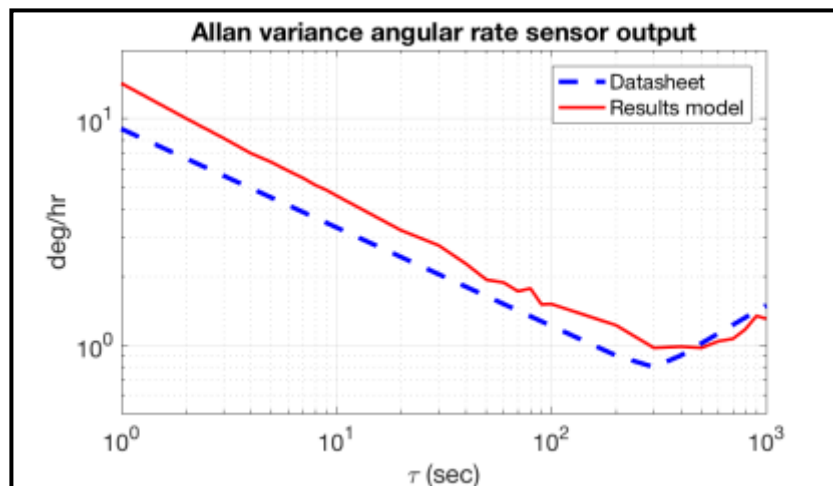


Figure 4-3: Allan variance model Gypro2300

The previous results presented show that the curves obtained with the simulation of the models are similar to those of the datasheets, and consequently, verify the correctness of the gyro model developed.

### 4.1.3. Angular rate sensor performance relative to a long term (satellite in eclipse).

Through eclipse, gyroscopes are required for attitude determination due the non-possibility to use sun sensors. The maximum eclipse time is 35 minutes; however, a worse-case eclipse period of 45 minutes is considered, this time include sensor calibration and enough time to recover the use of Sun sensors. The total pointing error required is of  $5^\circ$ , considering  $1^\circ$  as an expected control error, leaves  $4^\circ$  as a maximum attitude error at the end of an eclipse. Next simulations with sensors parametrized in 4.1.1 show the attitude error during the worse-case eclipse period. The objective is to identify a gyroscope suitable for the use in the R-3A with a maximum attitude error at the end of eclipse below of  $4^\circ$ .

#### 4.1.3.1. ADIS16135

Figure 4-4 shows ten simulations results for the ADIS16135 sensor, and it can be observed that the angular position error for this sensor goes beyond the required  $\pm 4^\circ$  pointing accuracy. This sensor differs from the other two sensors simulated that includes digital filters inside the component.

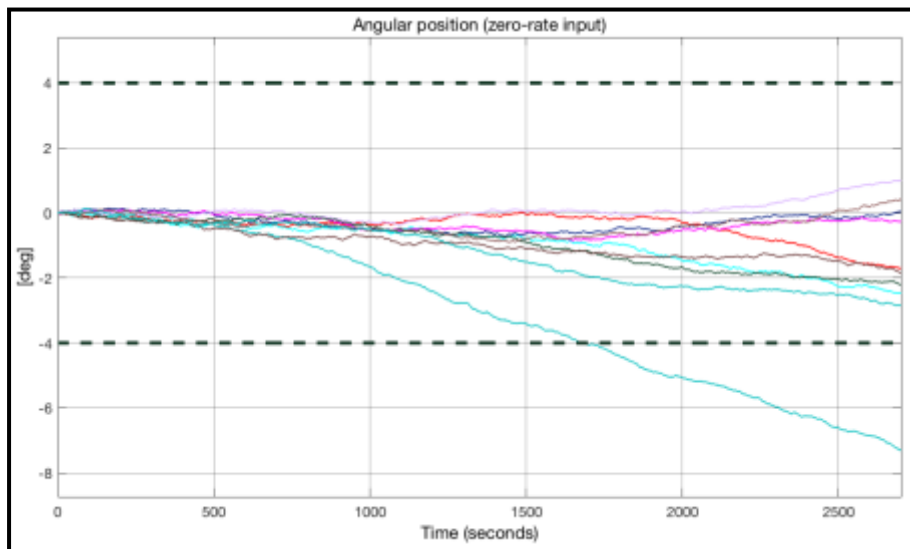


Figure 4-4: ADIS16135 angular position results for 45 minutes with zero-rate input

#### 4.1.3.2. CRM200

The ten results for the sensor CRM200 are plotted in Figure 4-5, the results for this sensor are very bad and exceed by great distance the range of  $\pm 4^\circ$ .

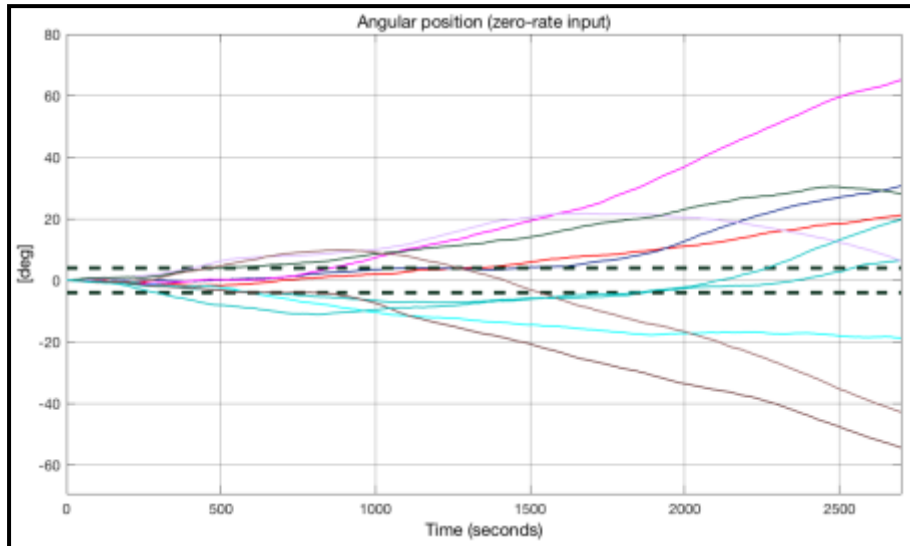


Figure 4-5: CRM200 angular position results for 45 minutes with zero-rate input.

#### 4.1.3.3. GYPRO2300

The ten responses for the GYPRO2300 can be seen in Figure 4-6, during the worse-case eclipse time the angular position error is inside the range of  $\pm 4^\circ$ .

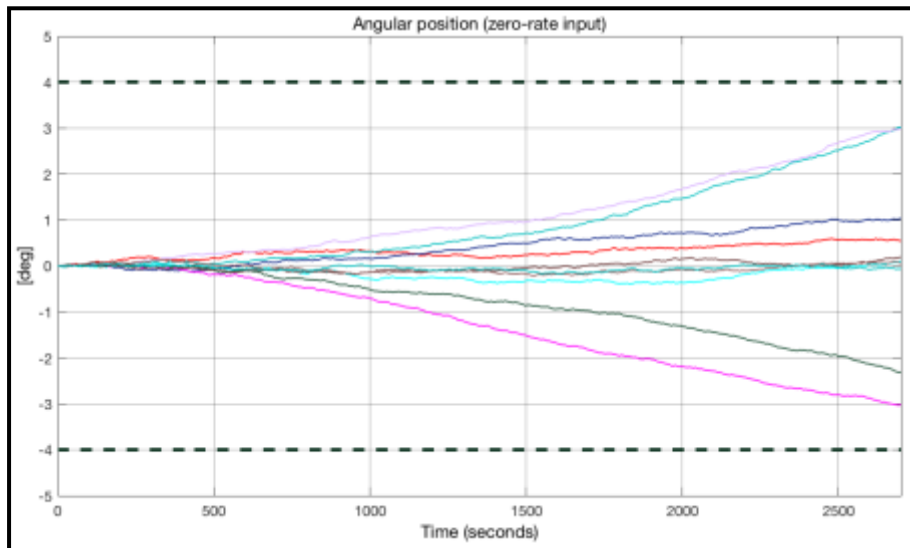


Figure 4-6: GYPRO2300 angular position results for 45 minutes with zero-rate input

In conclusion, the results for the GYPRO2300 show that this sensor is suitable for attitude determination during the worse-case eclipse time. In regard the ADIS16135, its results display that it may be used if additional filters are added to reduce the error of the signal.

## 4.2. Reaction wheel simulations

### 4.2.1. Parameters

Table 4 list the parameters used for the detailed model of the reaction wheel. RW parameters are used to represent the behaviour of the Small wheel from CubeSpace [35]. The EC-10 BLDCM parameters from a Maxon motor [36], are used to verify the correctness of the model. Table 5 shows the parameters used with the simplified model.

Table 4: Parameters used with detailed RW model

Parameters	RW <sup>3</sup>	EC-10 BLDCM
Moment of inertia [Kgm <sup>2</sup> ]	0.000002029	$8 \cdot 10^{-9}$
Stator resistance [ $\Omega$ ]	3	38.8
Stator inductance [H]	0.0001	$0.277 \cdot 10^{-3}$
Friction viscous coefficient [Nm/rad/s]	0.00000265	$9.09 \cdot 10^{-8}$
Back EMF [V/rad/sec]	0.0042	$1.879 \cdot 10^{-3}$
Number of poles	4	4
Supply voltage [V]	5	4
No load speed [rpm]	8000	16800

Table 5: Parameters used with simplified RW model

Parameters	Values
Moment of inertia [Kgm <sup>2</sup> ]	0.000002029
Winding coefficient	$2.747 \cdot 10^{-7}$
Friction viscous coefficient [Nm/rad/s]	0.00000455
No load speed [rpm]	8000

### 4.2.2. Simulations with “open-loop” model of RW.

The open-loop is used to evaluate the correctness of the model, analyse the response without any control and to determine the expected results when the controller is added.

<sup>3</sup> Some parameters are changed to obtain results as small wheel. J is the moment of inertia of the motor coupled with the moment of inertia of the flywheel [kg.m<sup>2</sup>];

Figure 4-7 shows the expected back EMF and the current of each phase, and the torque produced by the motor.

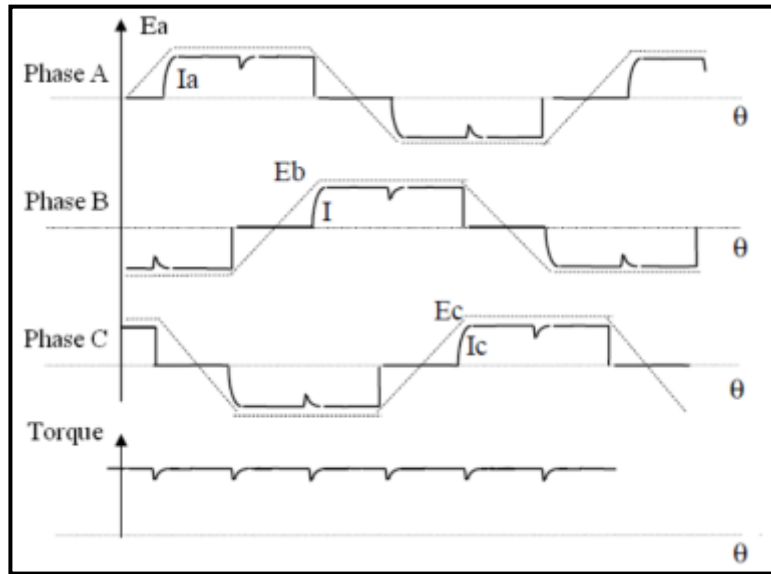


Figure 4-7: Expected current waveforms and torque with trapezoidal commutations [19].

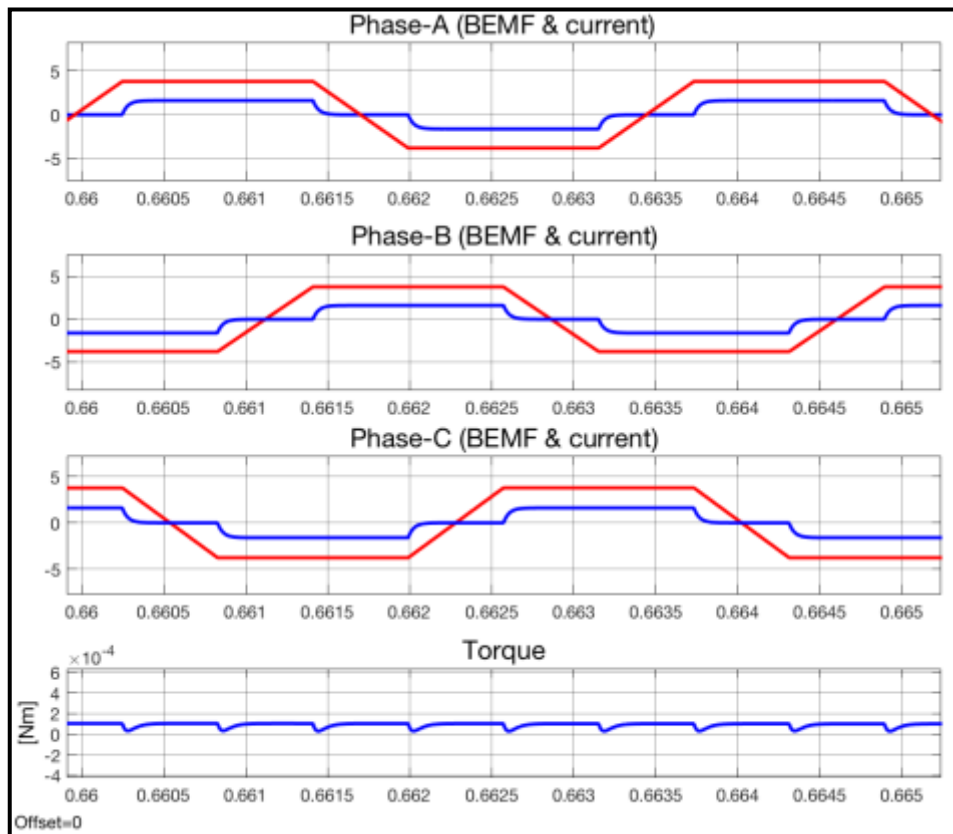


Figure 4-8: Current, back EMF and torque for open loop model

The results of the model, Figure 4-8, verifies that the BLDC motor is modeled correctly, giving the expected results of Figure 4-7. The model doesn't experiment the peak in the current, due to the assumption that each phase current is independent. It can be verified the sentence in 3.2.1.4, that the phase current is not established instantaneously, due to the "charge" and "discharge" of the inductor, and as a result, the torque produced by the motor has ripple.

The results of the model of the switching sequence in Figure 4-10 and of the hall sensor signals in Figure 4-9 verify Table 1.

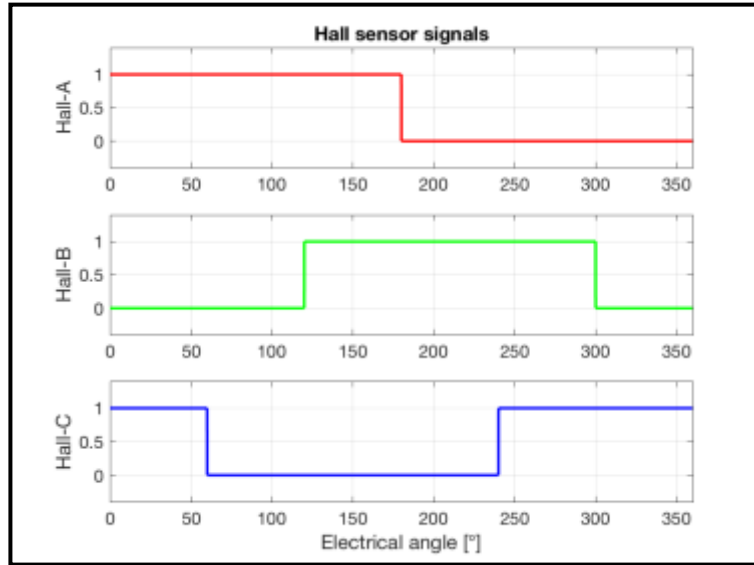


Figure 4-9: Hall sensor signals

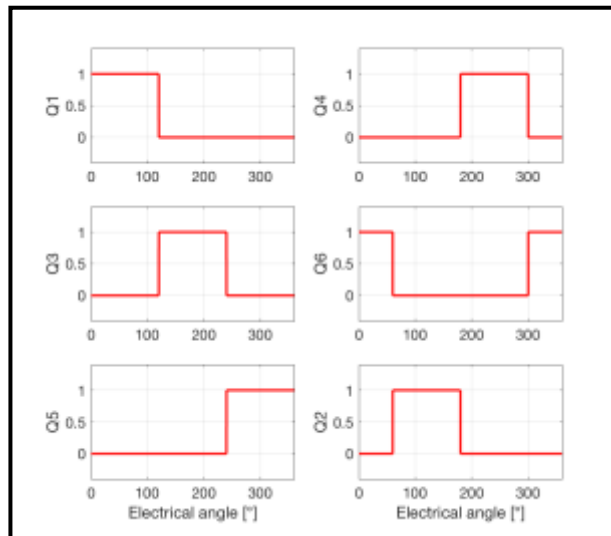


Figure 4-10: Control switching signals clockwise rotation

Figure 4-11 shows the results of the “open loop” model with the parameters for the RW. The parameters used give maximum speed as small wheel’s datasheet, i.e. 8000 rpm.

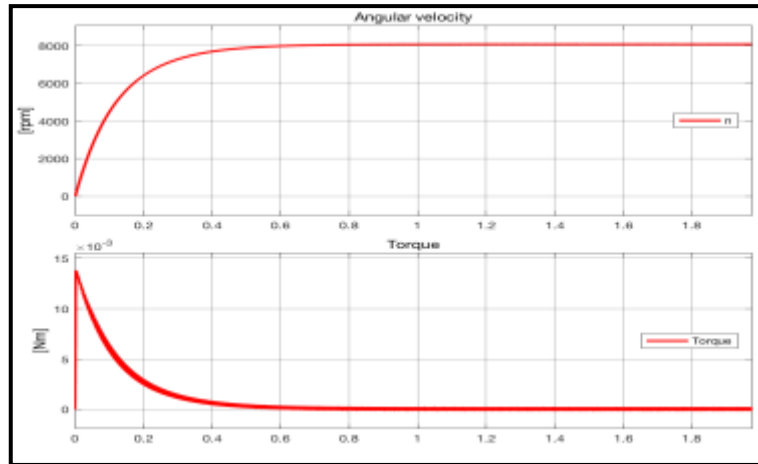


Figure 4-11: Open loop results with RW motor

Simulations with Maxon motor parameters, results in Figure 4-12, show that the model can be parametrized with values from BLDC's datasheets and get correct responses. The results show that the maximum speed for the model with these parameters is 16900 rpm, which is a value very close to the engine data sheet, that is 16600 rpm.

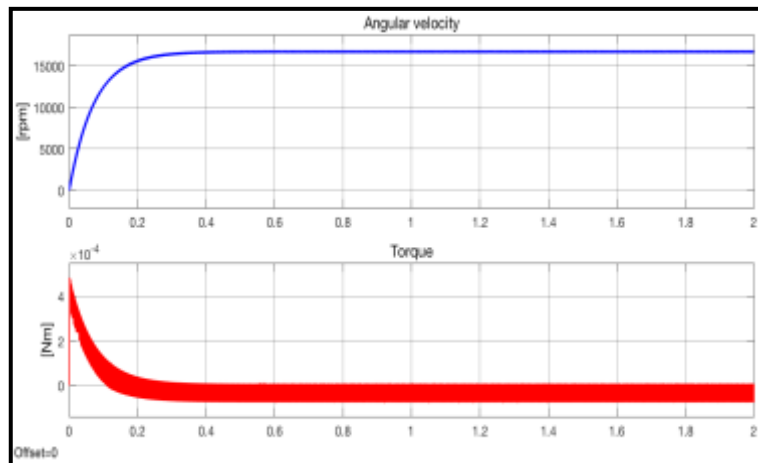


Figure 4-12: Open loop results of maxon motor

#### 4.2.3. Simulations with speed control model of RW

Figure 4-13 and Figure 4-14, show the back EMF and the current for each phase, and the torque produced by the wheel for the speed control model of RW. These results differ from those in the Figure 4-8 and Figure 4-7 that the current of each phase is limited by the PWM speed control, as well as the torque has more ripple produced by the controller aside from the generated by commutation.



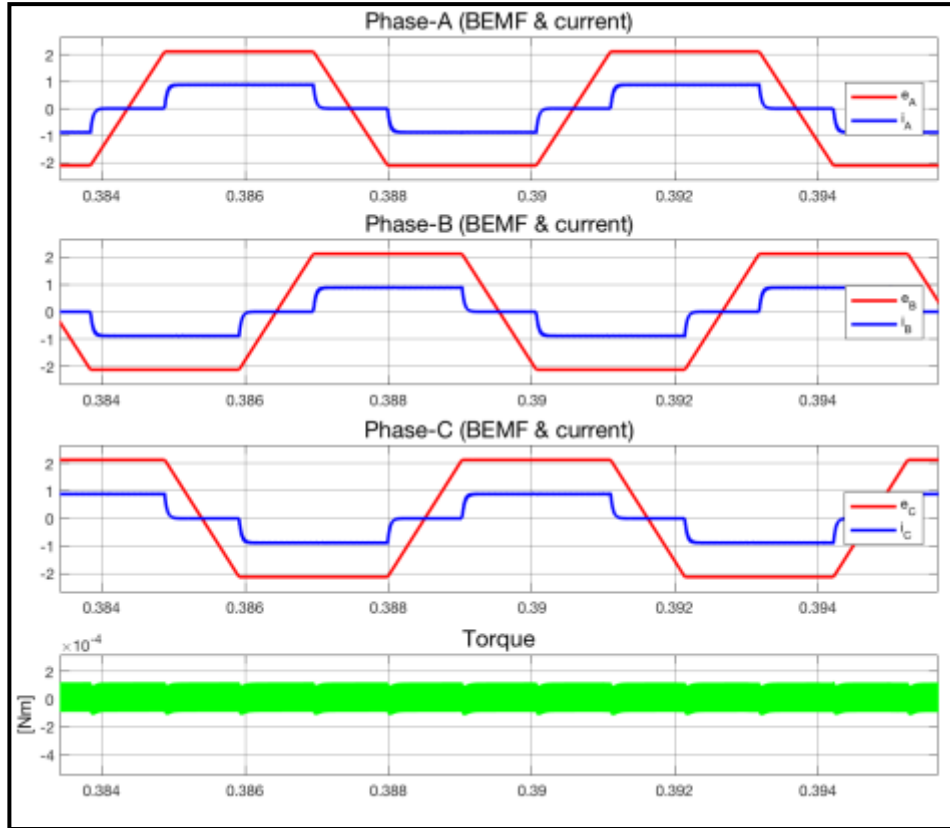


Figure 4-13: Current, back EMF and torque for speed controller model

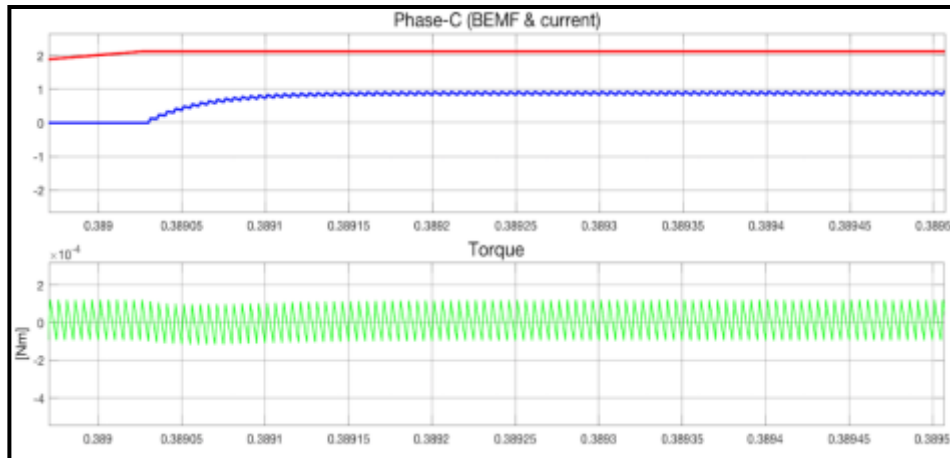


Figure 4-14: Zoomed view from Figure 4-13

Figure 4-15 presents the results for the reaction wheel model with speed controller, the desired speed is 5000 rpm which is achieved after 1.4 seconds. The torque of the RW is maximum at the beginning and has ripple. The shape of speed curve is due to the controller.

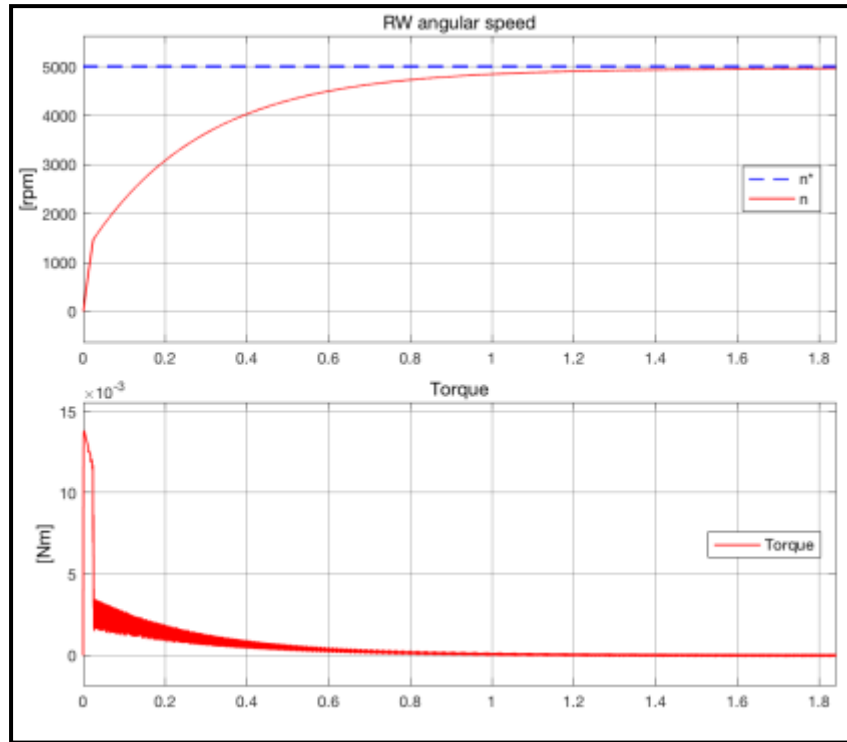


Figure 4-15: Open loop results of speed controller model

#### 4.2.4. Verification simplified model

It can be seen that the results obtained with the simplified model, Figure 4-16, coincide in shape with the complex model Figure 4-15, but it doesn't have torque ripple and has linear behaviour in contrast with the detailed model. Besides, the results show a setting time of 40 seconds in contrast with the 1.4 seconds of the detailed model. Instead, it is fast in simulations and can be used for the ADCS simulator.

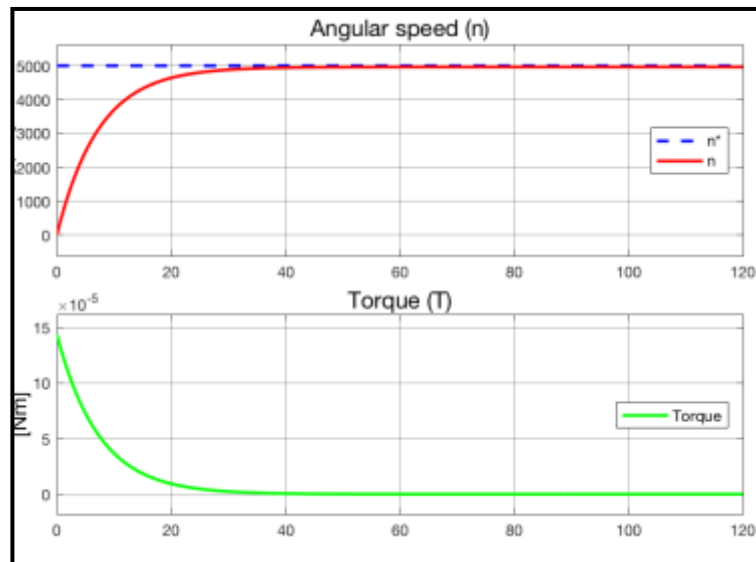


Figure 4-16: Results simplified RW model

### 4.3. RW-Satellite system dynamics simulations

The simplified model of a RW developed in 3.2.3 and the satellite model of section 3.3 are used to simulate the RW-Satellite system behaviour for different manoeuvre scenarios. Table 6 shows initial parameters for the different scenarios simulated. The moment of inertia of the R-3A satellite with the solar panels deployed, equation (4-2), parametrize the satellite model.

$$J_B = \begin{bmatrix} 0.04936 & 0 & 0 \\ 0 & 0.04929 & 0 \\ 0 & 0 & 0.02007 \end{bmatrix} \quad (4-2)$$

Table 6: Parameters for different scenario RW-Sat system simulations.

Parameter	Scenario 1	Scenario 2	Scenario 3	Scenario 4
Initial Angular velocity satellite ( $\vec{\Omega}_0$ )	=0	=0	=0	=0
Initial angular momentum RWs ( $\vec{h}_0$ )	=0	$n_x=2000$	=0	$n=3000$
Torques applied ( $\vec{T}_0$ )	=0	=0	5 mNm	=0
Change on angular moment RWs ( $\frac{d\vec{h}}{dt}$ )	$\neq 0$	=0	$\neq 0$	$\neq 0$

❖ Scenario 1 and 2: Changing speed of one RW

The first scenario simulates the results when the satellite is without angular movement, the reaction wheels are at zero speed, and one of them is accelerated until is saturated. The results in Figure 4-17 show the maximum speed reachable in the satellite around 2 deg/sec. However, the RW works at nominal speed; Figure 4-18 displays the highest speed on the satellite by accelerating one reaction wheel from nominal to maximum of around 1.5 deg/sec.

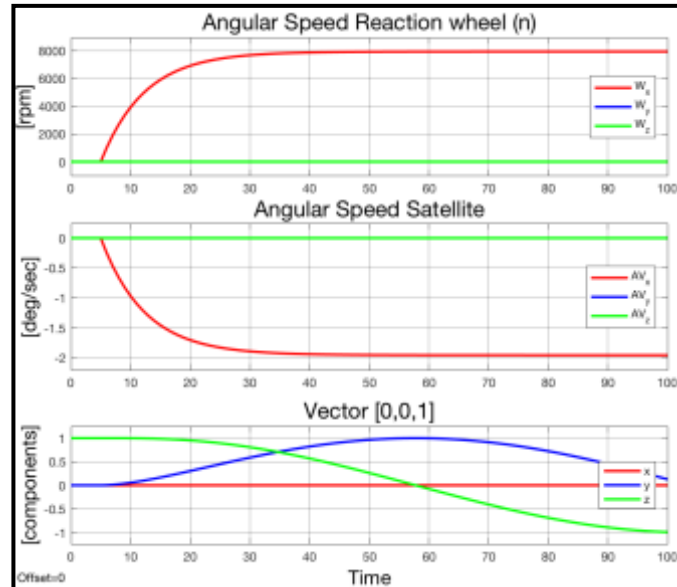


Figure 4-17: Results Scenario-1 of RW-Satellite system

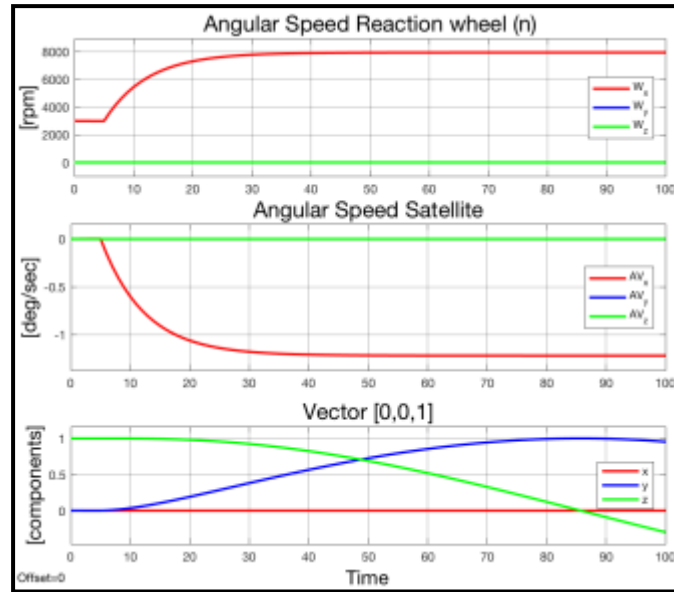


Figure 4-18: Results Scenario-2 of RW-Satellite system

❖ Scenario 3: Acceleration of RW with MTQ

This scenario represents the behaviour of the satellite when one RW is accelerated, and at the same time, one MTQ is active to create a torque to counteract the effect of the RW in the satellite. This process is done to settle the RW in nominal working speed. It is assumed that the MTQ applies a constant torque during the process of 5 mNm. With these conditions, it can be seen in Figure 4-19 that it will take around 1 minute to reach nominal speed in one RW. This procedure requires a controller to equalize the torque produced by the RW and by the MTQ and so avoid angular movement in the satellite while the procedure is done.

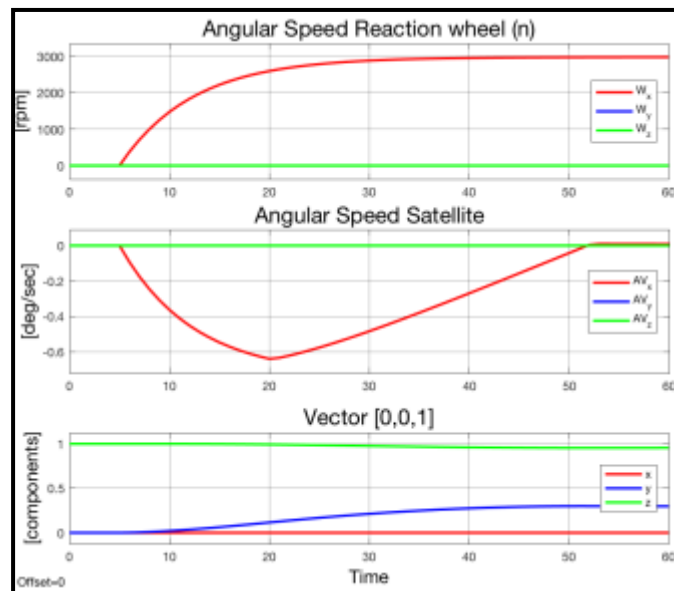


Figure 4-19: Results Scenario-3 of RW-Satellite system

❖ Scenario 4: Spin-stabilized with RWs spinning applying torques

In normal mode, the reaction wheels' work at nominal speed and by changing the speed of the reaction wheel a maneuver is done or a disturbance is counteracted. The following scenario simulated show the behaviour when the satellite has the RWs at nominal speed and one wheel is

accelerated to manoeuvre around x-axis. Figure 4-20 confirms that with this scenario the satellite will have swing motion due to the gyroscopic effect.

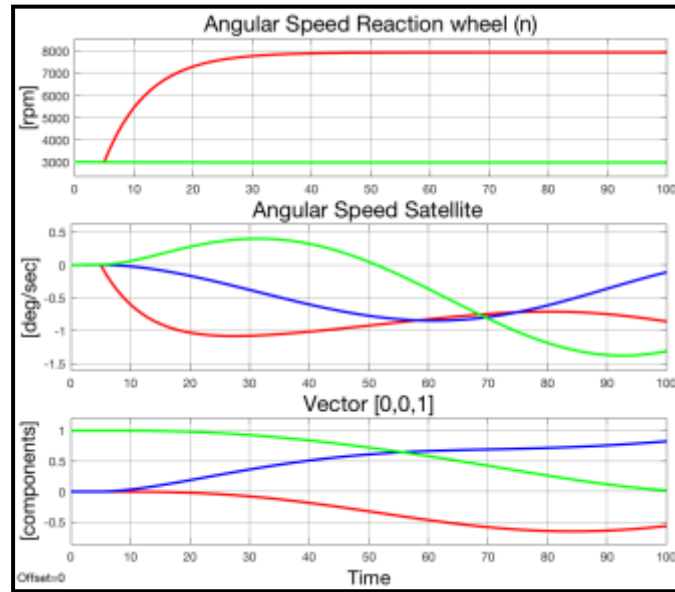


Figure 4-20: Results Scenario-4 of RW-Satellite system

❖ Scenario 1 with detailed model of RW

Figure 4-21 show the results of the simulations taken with the satellite model along with the detailed model of reaction wheel for the first simulation as Figure 4-17. Despite the differences between the RW models, there are no significant differences in the behaviour of the satellite model; the torque ripple is not big enough to cause appreciable effects. The differences are a different set time and that the maximum speed reachable by the satellite is smaller due to the RW does not reach 8000 rpm.

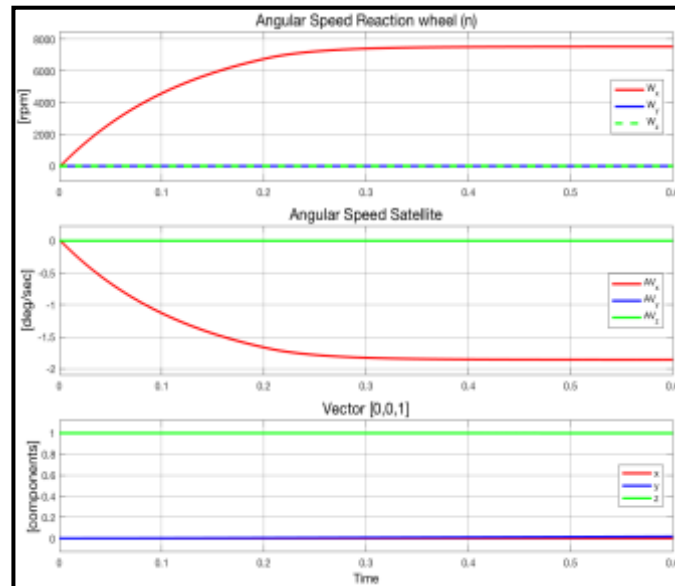


Figure 4-21: Results Scenario-1 of RW-Satellite system with detailed RW

---

## CHAPTER 5

---

# Conclusions

In this Master Thesis, models of angular rate sensors and reaction wheels are developed, verified and simulated in the context of R-3A. Through the literature review in Chapter 2, it was possible to recognise different models, evaluate them and select the one that was used. In Chapter 3, the model of the gyro was developed based on a real sensor with the errors sources that affect most in orbital conditions. Two models of RW were developed: a detailed model and a simplified model. The detailed model is based on an open loop model with a cascaded speed controller. The model includes the effects of viscous friction, commutation, and the controller. In contrast, the simplified model only includes the effect of friction. Besides, a model of the dynamics of a satellite is developed to analyse the effect of the RW in the satellite.

In Chapter 4, the simulations with the models were realised. The ARS model has been verified with the Allan variance method, proving that the model developed is correct. Then, three gyro sensors have been parametrised and simulated for the worse-case eclipse period; the results show that GYPRO is suitable for the use in the R-3A mission and that the ADIS sensor could be employed if additional filters are added. The RW detailed model has been verified using the expected curves for the current, the torque and the back EMF giving results according to the assumptions taken. Although the simulations prove that the detailed model is slow and cannot be used in the ADCS simulator, the model shows the effect of the commutation and the controller used. The simulations of the simplified model prove that is a fast model. Beyond, the results are quite similar to the detailed model to some extent, and thus this model can be used in the ADCS simulator. Finally, the simplified RW model is simulated along with the satellite model to back up the preliminary choice of RW in the context of the mission.

---

## CHAPTER 6 Works Cited

---

- [1] C. Montpellier, “Achievements and projects,” [Online]. Available: <http://csu.edu.umontpellier.fr/nanosatellites/realisations-et-projets/>. [Accessed 2017].
- [2] F. Hassen and E. Djamel , Multisensor Attitude Estimation, CRC Press, 2016.
- [3] M. C. Mahdi and M. C. Mahdi, “Attitude Determination and Control System design of KufaSat,” 2014.
- [4] L. M. F. and L. C. John, Fundamentals of Spacecraft Attitude Determination and control, Springer, 2014.
- [5] R. W. James, F. E. David and J. P. Jeffery, Space Mission Engineering: The New SMAD, Microcosm Press, 2011.
- [6] F. J. Kasper and V. Kasper , “Attitude Determination and Control System for AAUSAT3,” 2010.
- [7] European cooperation for space standardization, *Space engineering Gyro terminology and performance specification*, 2016.
- [8] C. J. L. W. J. L. a. W. Y. Liang Xue, “Noise Reduction of MEMS Gyroscope Based on Direct Modeling for an Angular Rate Signal,” *micromachines*, 2015.
- [9] A. Johan and J. Jimmie , “Improving the Inertial Navigation System of the CV90 platform using Sensor Fusion,” 2012.
- [10] C. J. L. W. T. X. a. W. Y. Liang Xue, “Analysis of Dynamic Performance of a Kalman Filter for Combining Multiple MEMS Gyroscopes,” *micromachines*, 2014.
- [11] L. M. F. and L. C. John, Fundamentals of Spacecraft Attitude Determination and control, Springer, 2014.
- [12] V. Carrara and H. K. Kuga, “Estimating Friction Parameters in Reaction Wheels for Attitude Control,” *Hindawi Publishing Corporation*, vol. 2013, no. 249674, p. 8, 2013.
- [13] V. Carrara, R. H. Siqueira and D. Oliveira, “Speed and current control mode strategy comparison in satellite attitude control with reaction wheels,” in *ABCM Symposium Series in Mechatronics - Vol. 5*, 2012, pp. 533-542.
- [14] V. Carrara and H. K. Kuga, “Current and Speed Control Operating Modes of a Reaction Wheel,” 2015.
- [15] M. R. Greene, “The Attitude Determination and Control System of the Generic Nanosatellite Bus,” 2009.
- [16] V. Carrara and H. K. Kuga, “Estimating friction parameters in reaction wheels for attitude control”.

- [17] S. Baldursson, "BLDC Motor Modelling and Control – A Matlab®/Simulink® Implementation," in *CHALMERS TEKNISKA HÖGSKOLA*, 2005.
- [18] M. Johansson, "Evaluation of Sensor Solutions & Motor Speed Control Methods for BLDCM /PMSM in Aerospace Applications," 2017.
- [19] A. Bilal and M. Bhardwaj, "Trapezoidal Control of BLDC Motors Using Hall Effect Sensors," Texas instrument, 2010.
- [20] B. Ø. Andresen, C. Grøn, R. H. Knudsen, C. Nielsen, K. K. Sørensen and D. Taagaard, "Attitude Control System for AAUSAT-II," 2005.
- [21] k. Sumitra and M. K. Giridharan, "Torque Ripple Minimization in Reaction Wheels Used in Satellites-A Comparison between Field Oriented Control of BLDCM and PMSM Using SVPWM," 1PG Scholar, Department of EEE, MBCET-Kerala, India, 2013.
- [22] S. Mondal, A. Mitra and M. Chattopadhyay, "Mathematical modeling and Simulation of Brushless DC motor with Ideal Back EMF for a Precision speed control," Kolkata.
- [23] G. Bara, "Comparative Study of Concentrated and Distributed Winding Using Flux," CEDRAT News, 2016.
- [24] "Permanent Magnet Machines for Hybrid and Electric Vehicles," 08 02 2013. [Online]. Available: <http://nptel.ac.in/courses/108103009/23>. [Accessed 06 2017].
- [25] P. Shiyong Lee, "A comparison study of the commutation methods for the three-phase permanent magnet brushless dc motor," Pennsylvania State University Berks Campus.
- [26] José Carlos Gamazo-Real, Ernesto Vázquez-Sánchez and Jaime Gómez-Gil, "Position and Speed Control of Brushless DC Motors Using Sensorless Techniques and Application Trends," Sensors, 2010.
- [27] R. P. G. Filipe, "Development of a reliable and low cost miniaturized Reaction Wheel System for CubeSat applications," 2016.
- [28] [Online]. Available: <https://base.xsens.com/hc/en-us/articles/203307252-Bias-repeatability-of-gyroscopes> .
- [29] M. Looney, " Anticipating and managing critical noise sources in mems gyroscopes ," 2012.
- [30] Mathworks matlab, "c2d," [Online]. Available: <https://se.mathworks.com/help/control/ref/c2d.html>. [Accessed 2017].
- [31] H. Munguia, "Introduction to digital filters," [Online]. Available: <http://paginas.fisica.uson.mx/>. [Accessed 2017].
- [32] H. S. M. G. H. C. D. K. K. J. S. R. Y. S. Jeon, "A New Simulation Model of BLDC Motor With Real Back EMF Waveform," Konkuk Univ.



- [33] M. Momenzadeh, A. Ahmed and A. Tolba, "Modelling and Simulation of The BLDC Electric Drive System Using SIMULINK/MATLAB for a Hybrid Vehicle," Universitat Paderborn, 2013.
- [34] M. Looney, " Designing for low noise feedback control with mems gyroscopes ," 2012.
- [35] CubeSpace, "CubeWheel Small satellite reaction wheels," [Online]. Available: <https://www.cubespace.co.za/cubewheel>. [Accessed 2017].
- [36] Maxon, "Maxon motors," [Online]. Available: <https://www.maxonmotor.com>
- [37] L. C. NG, "On the application of Allan Variance Method for Rings Laser Gyro Performance characterization," Lawrence Livermore National Laboratory, 1993.
- [38] IEEE-SA Standards Publications, "Guide and Test Procedure for Single- Axis Interferometric Fiber Optic Gyros," The Institute of Electrical and Electronics Engineers, Inc., 2008.
- [39] Freescale Semiconductor, "Allan Variance: Noise Analysis for Gyroscopes," 2015.
- [40] N. T. a. S. I. Roumeliotis, "Indirect Kalman Filter for 3D Attitude Estimation A Tutorial for Quaternion Algebra," 2005.
- [41] C. L. Dym, Principles of Mathematical Modeling, Elsevier Academic Press, 2004.
- [42] K. Ogata, Modern Control Engineering, Prentice Hall, 2010.
- [43] A. Heidecker, "Development of algorithms for attitude determination and control of the AsteroidFinder satellite," 2009.
- [44] California Polytechnic State University, "CubeSat Design Specification," 2009.
- [45] R. Walker, 11 April 2017. [Online]. Available: [http://www.esa.int/Our\\_Activities/Space\\_Engineering\\_Technology/Technology\\_CubeSats](http://www.esa.int/Our_Activities/Space_Engineering_Technology/Technology_CubeSats). [Accessed June 2017].
- [46] CubeSpace, *Cube Wheel*.

## APPENDIX A

### Allan variance

Allan variance is a time domain analysis technique that is applied to analyse the error characteristics of any precision measurement instrument [37]. The Allan variance is an accepted IEEE standard for fiber optic angular rate sensors specifications [38]. The Allan variance can be defined either in terms of the output rate or the output angle, the output of the model is output rate therefore the Allan variance is defined in terms of output rate. The Allan method assumes that the uncertainty in the data is generated by noise sources of specific character. The magnitude of each noise source covariance is then estimated from the data. The results from this method are related to five basic noise terms appropriate for inertial sensor data. These are quantization noise, angle random walk, bias instability, rate random walk, and rate ramp [39], Figure 1.

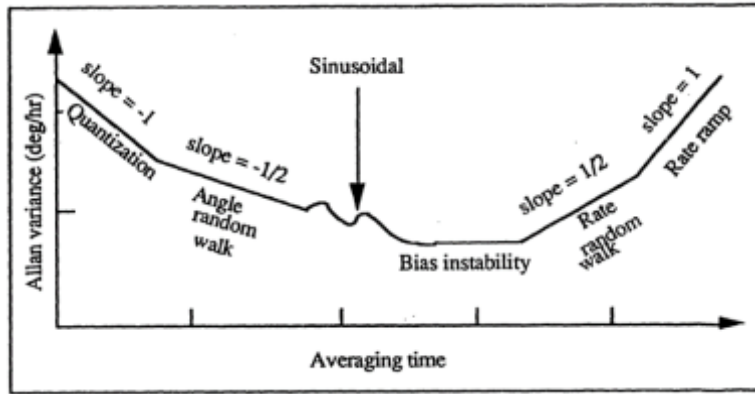


Figure 1: Sample plot of Allan variance results

A data stream is divided into clusters of specific length and the average value of each cluster is computed. A two-point sample variance is then calculated from the successive cluster averages. By choosing different cluster length or averaging time (correlation time) for each Allan variance computation, one obtains the Allan variance as a function of the averaging time. The attractiveness of this method is that the Allan variance, when plotted in logarithmic scales, can discriminate different contributing error sources by simply examining the varying slopes on the Allan variance plot. Furthermore, by picking specific values of averaging time, one can easily extract information from the error source. The typical averaging time scale for the computation of each component is: several tens of second of data for the quantization error, several minutes of data for angle random walk, several hours of data for bias instability, and several tens of hours of data for rate random walk and rate ramp.

#### Allan method [37]:

A collection of  $N$  consecutive angular rate data points is acquired with a rate of  $f_s$  samples per second. Then a  $k=N/m$  clusters are formed, where  $m$  is the averaging factor or the number of samples per cluster. The second step is to compute the average for each cluster from the Eq. 1

$$x_k(m) = \frac{1}{m} \sum_{i=1}^m x_{(k-1)m+i} \quad ; K = 1, \dots, k \quad \text{Eq. 1}$$

The third step is to compute the Allan variance from the cluster averages as follows Eq. 2:

$$\sigma^2(\tau_m) = \frac{1}{2(k-1)} \sum_{k=1}^{k-1} (x_{k+1}(m) - x_k(m))^2 \quad \text{Eq. 2}$$

Where  $\tau_m$  is the specified averaging time defined in equation Eq. 3

$$\tau_m = \frac{m}{f_s} \quad \text{Eq. 3}$$

Finally, in Eq. 4 take the square root of the result obtained to obtain the value of the root Allan variance or the Allan deviation for a particular value of  $\tau_m$ :

$$\sigma_y(\tau_m) = \sqrt{\sigma_y^2(\tau_m)} \quad \text{Eq. 4}$$

The described sequence of steps yields the estimated value of the Allan deviation for the chosen averaging time  $\tau_m$ . In order to obtain the whole curve, the computation is repeated multiple times for a sequence of  $\tau_m$  values and is plotted as a loglog plot. The block is done by a Matlab function, the code is showed in Figure 2.

```
function ALLAN(data fs)

%Input:
%fs is sampling frequency
%data is the data from the gyroscope

%Detect number of samples (N) of data
[N M] = size(data);
%create variables
AllanV=zeros(73,1);
Tt=zeros(73,1);

%calculation with different averaging factor m
m=200;
for n=1:50

    %Save data to X
    X=data(:,n);
    %t0 = sample time
    t0 = 1/fs;
    %Calculate the number of clusters
    z=fix(N/m);
    %create variable
    Dff=zeros(z,1);
    %Create a matrix to save averages
    mean_x=zeros(z,1);
    x=zeros(z,1);

    for k=1:z
        %average for each cluster
        if k==1
            mean_x(1)=mean(X(1:100));
        else
            mean_x(k)=mean(X(m*(k-1):m*k));
        end
        x(k)=mean_x(k);

        %calculate difference between averages
        if k~=1
            Dff(k-1)=(x(k)-x(k-1))^2;
        end
    end
end
```

```
%Calculate the Allan variance for averaging factor
AllanV(n)=sqrt(sum(Dff)/(2*(z-1)))*3600;
%Quasi time T
Tt(n)=(t0* m);

%change m
if n<10
    m= m+200;
elseif n<19
    m= m+2000;
else
    m= m+20000;
end
end

%plot
figure(6)
set(gca,'font size',30)
loglog([1,200,300,400,1000],[9,0.9,0.8,0.9,1.5], '--
','LineStyle','Color','b')
xlabel('(\tau) (sec)','font size',16)
ylabel('deg/hr','font size',16)
title('Allan variance angular rate sensor output','font size',20)
xlim([1 1000]);
ylim([0.5 20]);
set(gca,'font size',15)
grid on
hold on

%loglog([1,200,300,1000],[5.5,0.64,0.6,0.7], '--
','LineStyle','Color','g')
loglog(Tt,AllanV,'LineStyle',2,'Color','r')
hold off

end
```

Figure 3: Allan variance Matlab code

---

## APPENDIX B

---

# Attitude quaternions

The attitude can be described by different methods such as Euler angles, direction cosine matrices or quaternions, in this report quaternions are used. The quaternion can be obtained from the angular velocity from equations Eq. 5 and Eq. 6. [40]

$$Q_k = Q_{k-1} + \Delta t \cdot \frac{1}{2} [\Omega(\Omega)] \cdot Q_{k-1} \quad \text{Eq. 5}$$

$$[\Omega(\Omega)] = \begin{bmatrix} 0 & \Omega_z & -\Omega_y & \Omega_x \\ -\Omega_z & 0 & \Omega_x & \Omega_y \\ \Omega_y & -\Omega_x & 0 & \Omega_z \\ -\Omega_x & -\Omega_y & -\Omega_z & 0 \end{bmatrix} \quad \text{Eq. 6}$$

## APPENDIX C

# Matlab/Simulink implementation

## I. Gyroscope model Simulink implementation

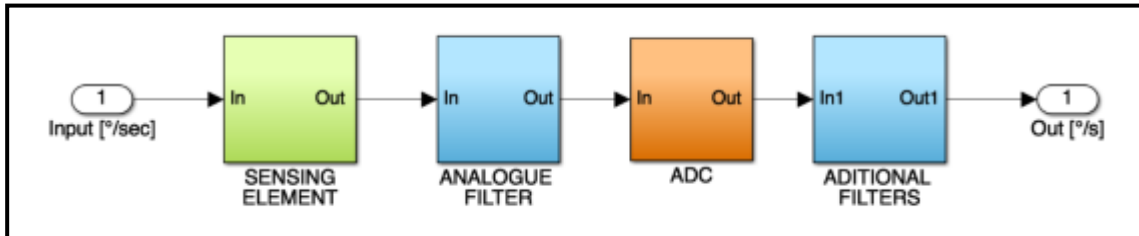


Figure 4 Internal Black box model view

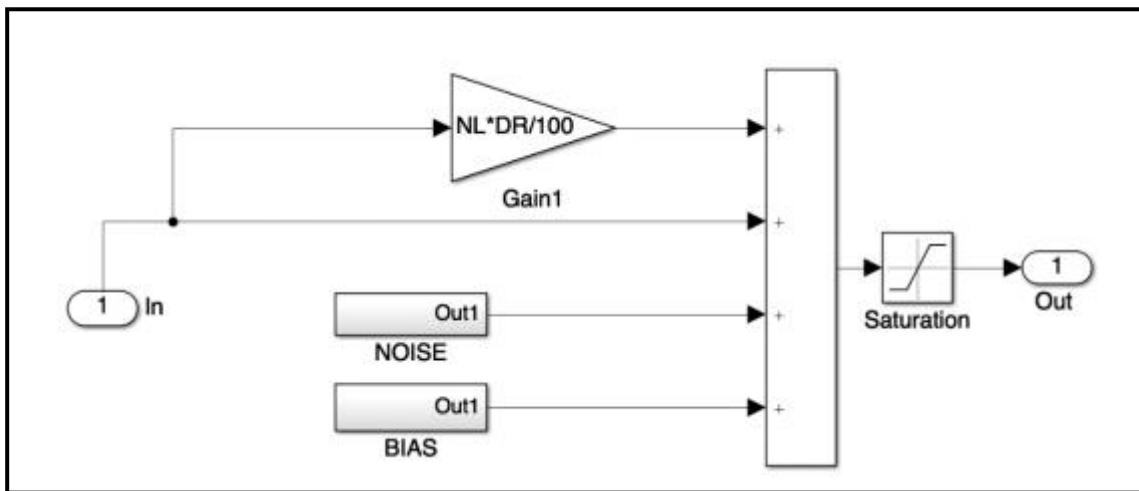


Figure 5 Sensing element module implementation

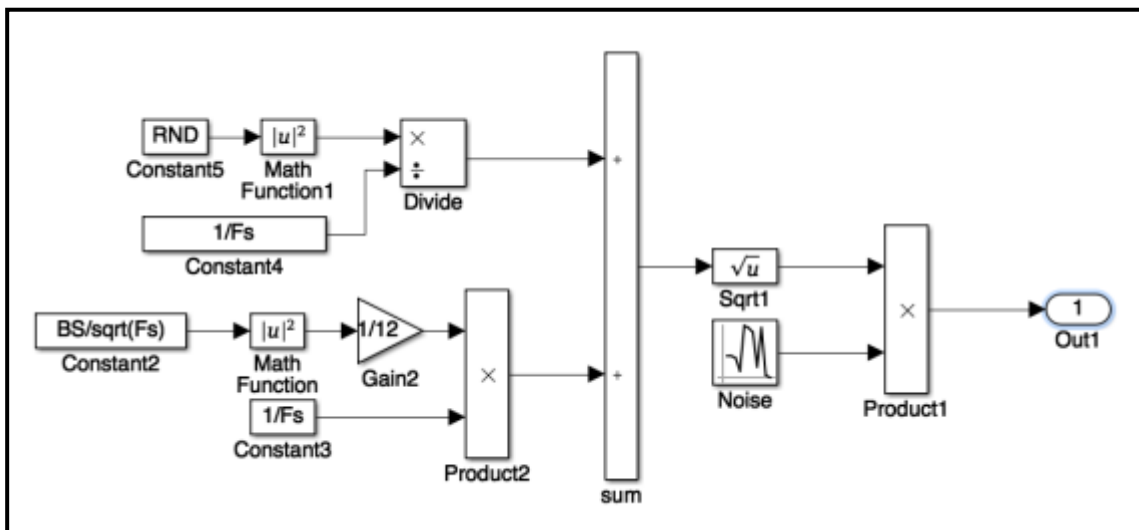


Figure 6: Noise block

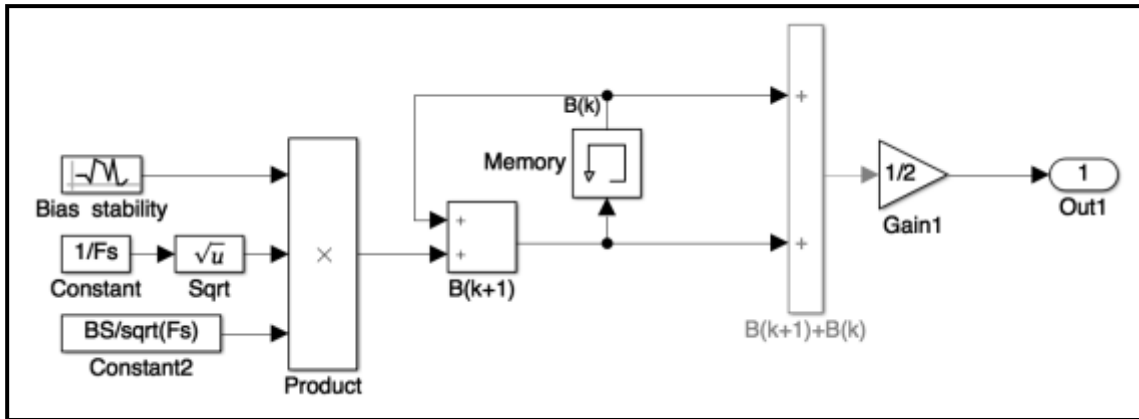


Figure 7: Bias block

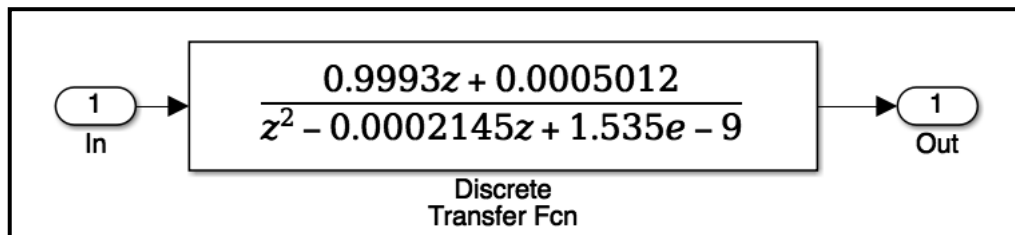


Figure 8: Analogue filter module implementation

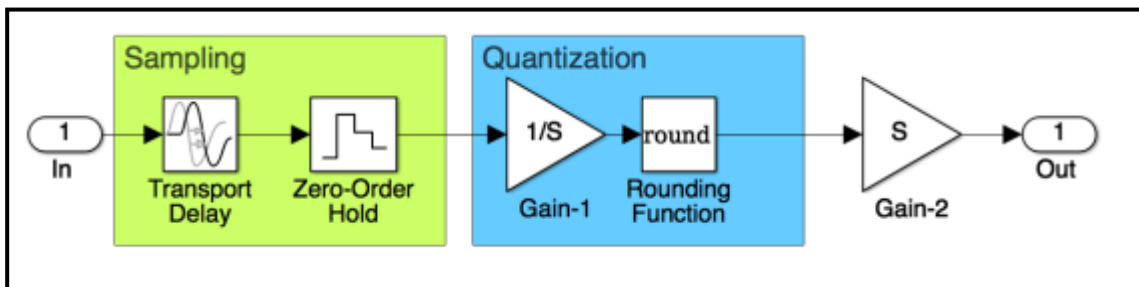


Figure 9: ADC module implementation

## II. Detailed reaction wheel model Simulink implementation

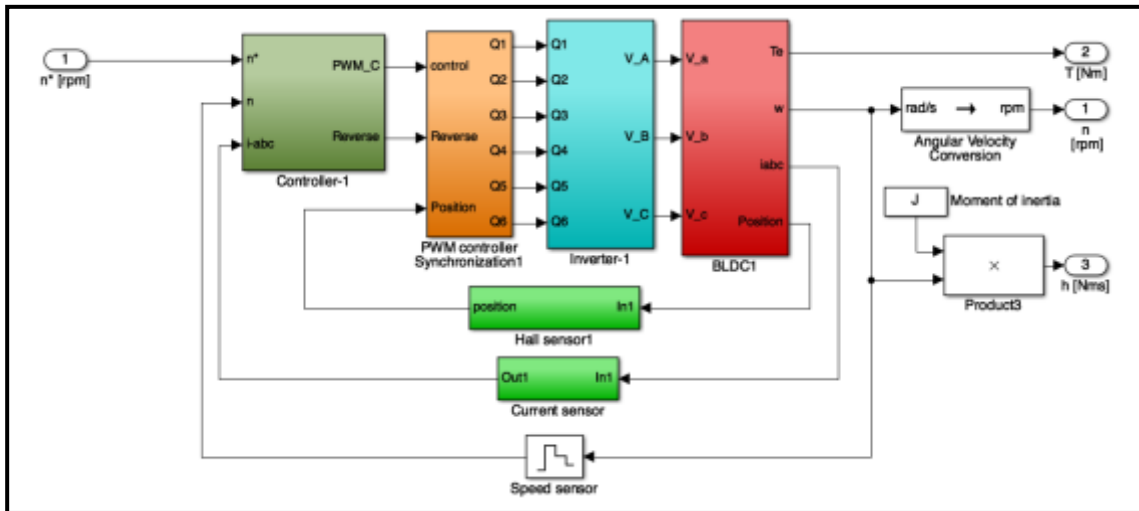


Figure 10: Internal Black box model view

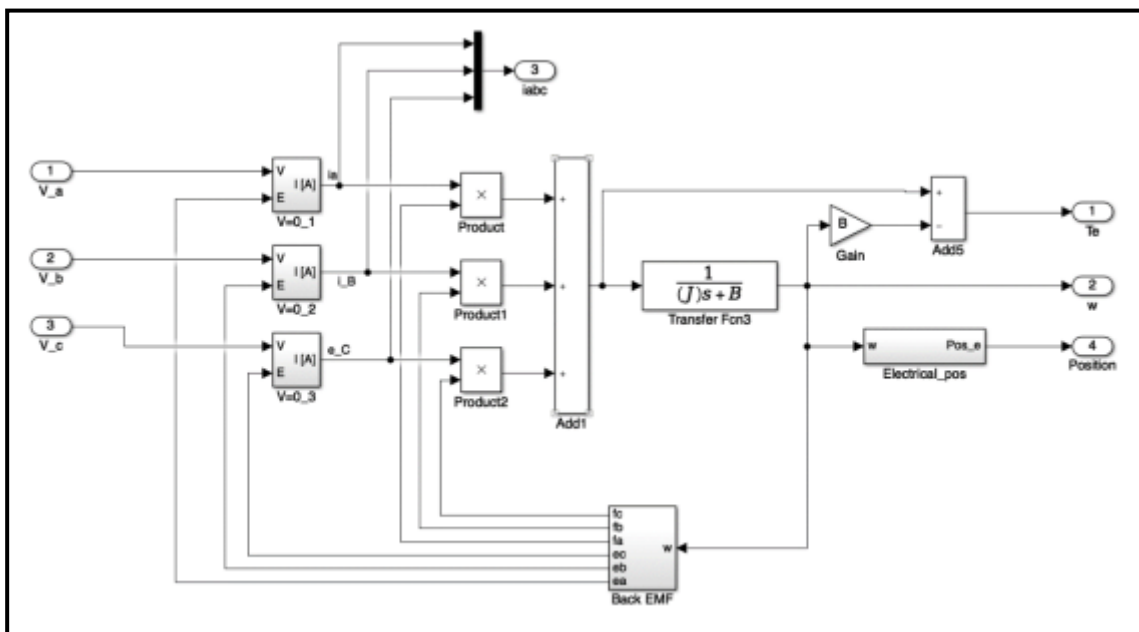


Figure 11: BLDC motor block



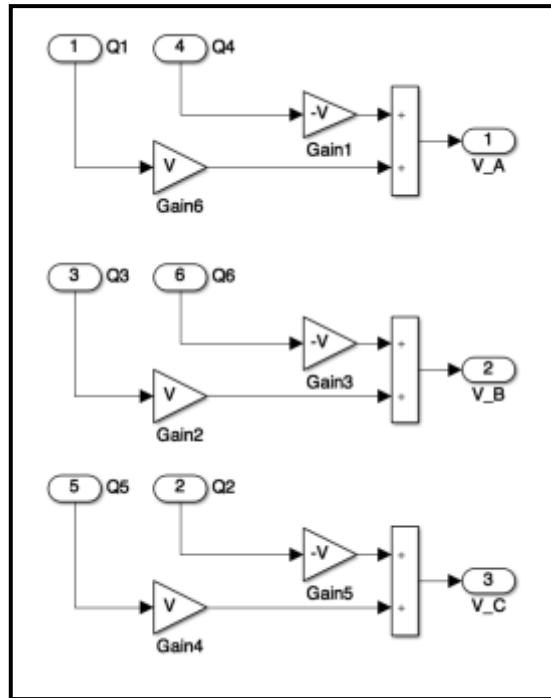


Figure 12: 3-phase inverter circuit block

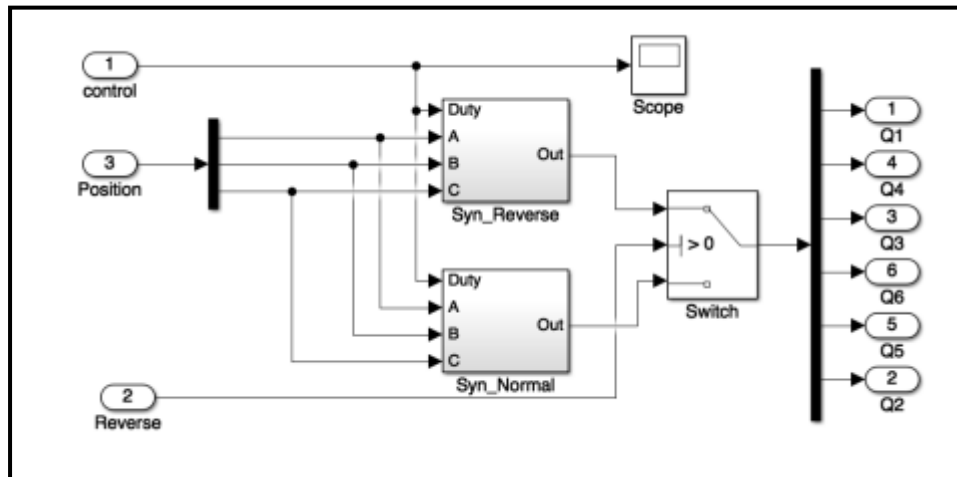


Figure 13: Commutation block

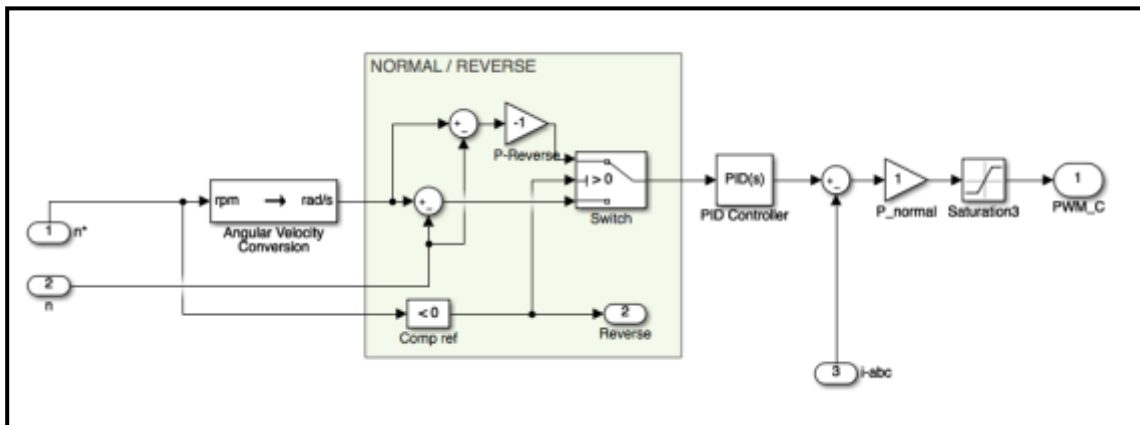


Figure 14: Speed controller block

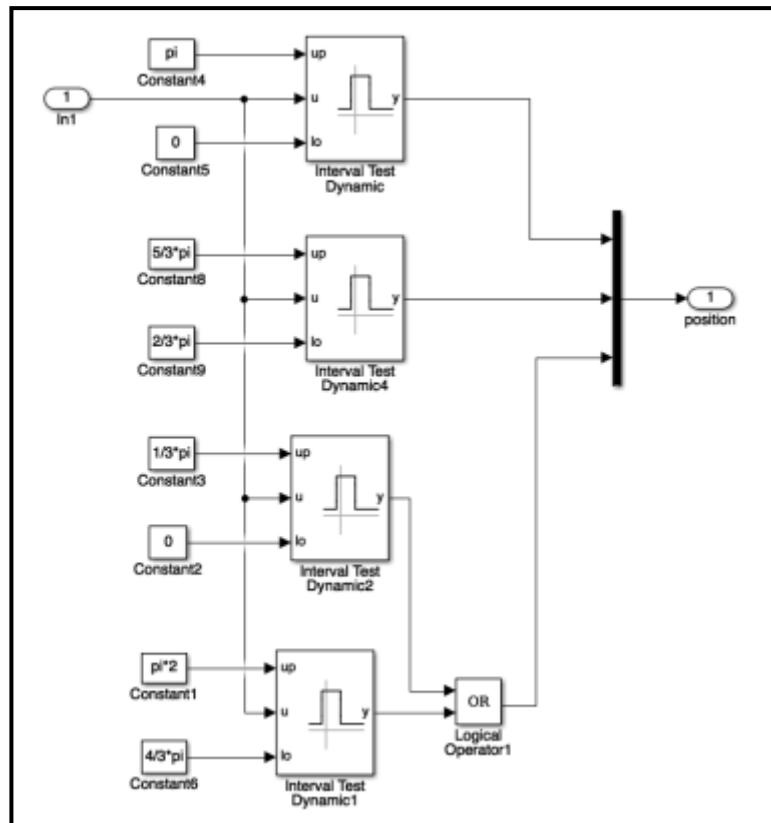


Figure 15: Hall sensor block

### III. Simplified reaction wheel model Simulink implementation

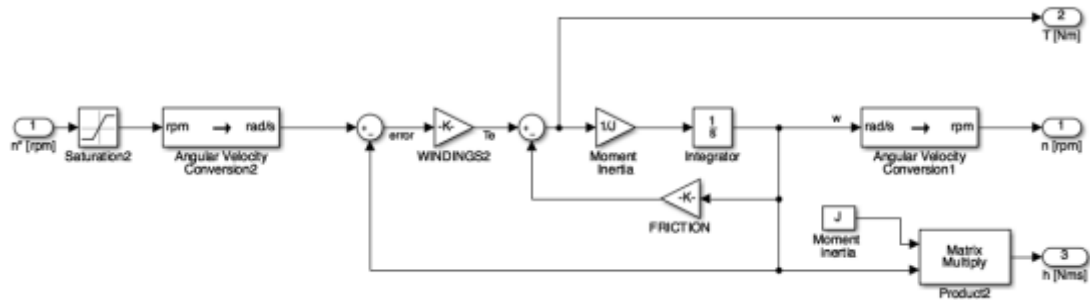


Figure 16: Internal black box model view

## IV. Satellite dynamics model Simulink implementation

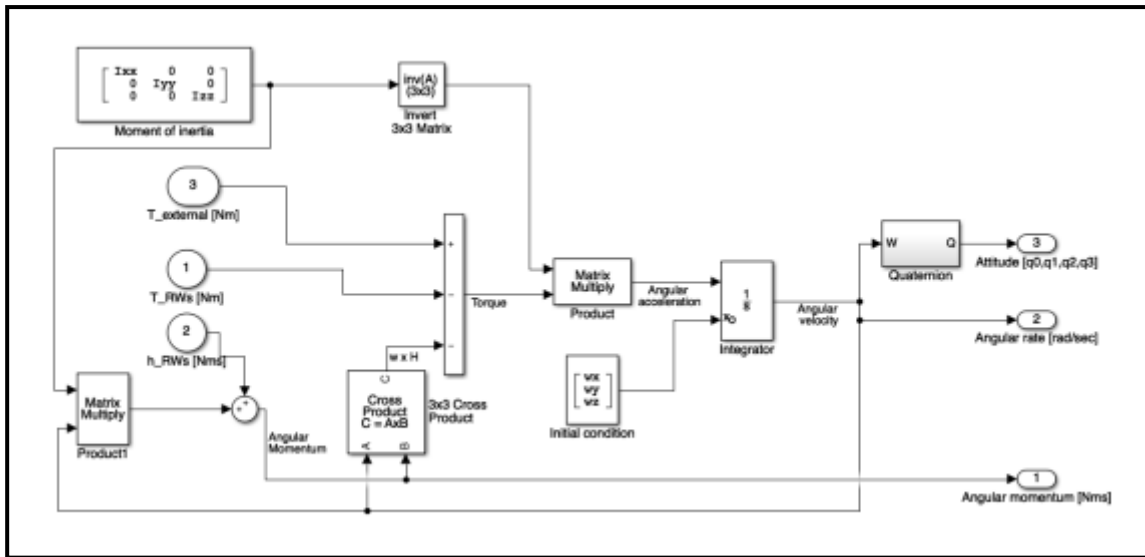


Figure 17: Internal black box model view